EVOLUTION OF DUST TRAILS INTO BANDS

D. Vokrouhlický,[1] D. Nesvorný, AND W. F. Bottke

Southwest Research Institute, 1050 Walnut Street, Suite 300, Boulder, CO 80302

ABSTRACT

We use numerical simulations to investigate the production of dust trails by asteroid disruption events. Our work shows that asteroid trails evolve into pairs of dust bands over time. Coherent trails typically survive several tens of kyr before evolving into complete bands after ∼1 Myr. The transition timescale depends sensitively on the location of the source breakup event in the main asteroid belt. Bands develop more efficiently from sources in the middle/outer belt than in the inner belt, which may not produce observable pairs of bands at all. The infrared structures produced by recent disruption events (<1 Myr) are characterized by a complicated and changing set of incomplete arcs and cusps. Their geometry depends both on the observer's position and on the source's location in terms of heliocentric distance and inclination to the ecliptic. We postulate that the broad orphan trails named C and D by Sykes in 1988 might have been produced by the formation of the Datura asteroid family 450 ± 50 kyr ago. Additional work will be needed to test this link.

Subject headings: celestial mechanics — infrared: solar system — interplanetary medium

Online material: color figure

1. INTRODUCTION

The circumsolar dust cloud, known also as the Zodiacal Cloud (ZC), is the most prominent source of thermal radiation in the solar system except for the Sun itself. This is because the particles of the ZC, even though they have negligible total mass, have a total cross-sectional area capable of absorbing and re-emitting an enormous amount of radiation from the Sun. Observations of dust in young exoplanetary systems provide additional examples of this effect, and dust can be diagnostic of the presence of embedded planets or disruptions of large planetesimals (e.g., Telesco et al. 2005).

There has been considerable debate about whether comets or asteroids provide most of the dust residing in the ZC (see discussions in recent reviews by Dermott et al. 2001, 2002a; Sykes et al. 2004). While modeling work of the large-scale ZC particle distribution allows us to glean many useful insights into this question (e.g., Kelsall et al. 1998; Hahn et al. 2002), complementary constraints can be found by analyzing small-scale structures detected in data from the *Infrared Astronomical Satellite* (*IRAS*). These structures mainly consist of pairs of dust bands (Low et al. 1984; Dermott et al. 1984) and dust trails (Sykes et al. 1986; Sykes 1988). Each is discussed below.

Interplanetary dust bands, first discovered in the all-sky infrared data taken by *IRAS* as local maxima of the infrared flux nearly parallel to the ecliptic when smooth background flux was filtered out (Low et al. 1984), consist of a toroidal distribution of dust particles slightly inclined to the ecliptic. They are produced by orbits sharing the same proper inclination and both forced inclination and nodes; proper nodes are randomized between 0° and 360°. Dust bands are believed to be associated with disruption events in the main asteroid belt (e.g., Low et al. 1984; Dermott et al. 1984). Based on a comparison between the inclinations of the most prominent *IRAS* dust bands and those of the large asteroid families Themis, Koronis, and Eos, Dermott et al. (1984) suggested that the bands may well be features produced by the

continuous collisional grinding of fragments within these families. If true, these bands would be hundreds of Myr to several Gyr old. Advances in our understanding of asteroid breakups, however, now suggest alternative source regions. Prominent pairs of *IRAS* bands previously linked to Koronis and Eos instead were produced by the breakup of individual asteroids over the last 10 Myr, consistent with the stochastic formation model first advocated by Sykes & Greenberg (1986). One pair of bands comes from the Karin cluster, a small asteroid family produced by the breakup of a $D \sim 33$ km parent body 5.75 ± 0.05 Myr ago (Nesvorný et al. 2002, 2003, 2006a, 2006c; Nesvorný & Bottke 2004). A second pair of bands comes from the Veritas family, which was produced by the disruption of a 170 km asteroid 8.3 ± 0.5 Myr ago (Dermott et al. 2002b; Nesvorný et al. 2003). Both the Karin and Veritas families are more than 2 orders of magnitude younger than the prominent families mentioned above (e.g., Vokrouhlický et al. 2003, 2006a, 2006b). The Veritas family also provides a better match to the observed inclination of the 10° band than the Eos family (e.g., Dermott et al. 2002b; Nesvorný et al. 2006c).

Dust trails are generally thought to have been formed by active comets. Comet trails are produced by particles hundreds of microns to millimeters in diameter released from a cometary surface within the last 100 yr or so. As such, the trails consist of particles residing on nearly identical orbits (similar to that of the parent object) with only a slight dispersion of orbital parameters due to evolution by radiation forces. For a parent body of a highly eccentric orbit only part of the trail might be observable from existing telescopes. However, incomplete trails that do not extend angularly over 360° are also produced by a very recent dust ejection of particles that did not disperse along the whole orbit. Several trails discovered in *IRAS* sky scans have been matched to the orbits of known comets (Sykes 1988; Sykes & Walker 1992). Additional links have been made using observations in visual wavelengths (e.g., Nakamura et al. 2000; Ishiguro et al. 2002) and those from the *Infrared Space Observatory* (*ISO*; e.g., Davies et al. 1997; Reach et al. 2000).

Sykes (1988) and Sykes & Walker (1992) also identified several so-called orphan dust trails in the *IRAS* data set that could not be linked to any known comet. They speculated that these trails

[1] On leave from Institute of Astronomy, Charles University, V Holešovičkách 2, 18000 Prague 8, Czech Republic.

might correspond to recently disintegrated comets or comets that had been so recently scattered by Jupiter that the orbit of the trail would be different from that of the comet. More recently, Nesvorný et al. (2006d) used data from the *Spitzer Space Telescope* to identify three dust trails. The narrowest trail was unambiguously linked to the comet 29P/Schwassmann-Wachmann 1. The source of the two broader trails, however, was less clear. These two *Spitzer* trails were linked to two of the orphan *IRAS* trails (A and B) described by Sykes (1988) and Sykes & Walker (1992). Using both *Spitzer* and *IRAS* data sets, Nesvorný et al. (2006d) had enough information to determine the approximate orbits of these trails. Surprisingly, they found that the trails had to come from sources inside the main asteroid belt. Moreover, the broad structure and strength of these trails led them to propose that they were not produced by members of a new class of comet-like objects embedded in the asteroid belt (see, e.g., Hsieh et al. 2004; Hsieh & Jewitt 2006), but instead were most likely the outcome of two very recent asteroid disruptions. Accordingly, this would mark the first time that dust trails have been linked with asteroid sources.

What events could produce these trails? Nesvorný et al. (2006b) and Nesvorný & Vokrouhlický (2006), using a new identification technique, have discovered evidence for asteroid clusters produced by disruptions of ∼10 km sized parent bodies approximately 100–500 kyr ago. It is likely that even younger clusters will be discovered as our knowledge of the main belt population increases with time (e.g., a boom in asteroid discovery rate is expected from the Panoramic Survey Telescope and Rapid Response System (Pan-STARRS) project; Jedicke et al. 2007). These discoveries raise questions about the infrared structures expected for dust produced by very recent asteroid disruptions. Sykes & Greenberg (1986) and Sykes et al. (1989) estimated a pair of dust bands should develop on a timescale of several hundred kyr to several Myr. This means that while older asteroid families can produce dust bands (e.g., Sykes 1988, 1990), younger ones might produce broad dust trails.

Motivated by these recent discoveries, our goal in this paper is to model how dust produced immediately after an asteroid disruption evolves collisionally and dynamically from a dust trail to a pair of dust bands. Specifically, we assume that the dust is produced at orbit locations corresponding to several newly discovered asteroid clusters. We then determine: (1) the timescale over which detectable dust trails disperse, (2) the nature of dust-driven infrared structures in the transition phase prior to dust band development, and (3) the possibility of detecting these transient structures using space-based infrared telescopes like *IRAS* and *Spitzer*. Our approach to modeling the relevant processes is described in § 2. Application of our method to dust production from four interesting asteroid-dust sources is described in § 3. The implications of our work are discussed in § 4.

2. MODEL DESCRIPTION

Our model consists of several components. First, we characterize the source event, defined as the breakup of an asteroid in the main belt. The related parameters are primarily the orbit of the parent object prior to disruption and the size distribution of the ejecta in the subcentimeter range. We neglect fragments larger or smaller than a particular range of diameters because they do not contribute significantly to the total infrared flux. These initial ejecta are allowed to evolve over a chosen time span, typically ≲1 Myr. During this time, the fragments undergo orbital evolution from planetary perturbations, radiation pressure, and Poynting-Robertson (P-R) drag. The P-R drag, produced by the radiation force component tangential to the orbit, makes the bodies spiral inward toward the Sun (Wyatt & Whipple 1950; Burns et al. 1979). The fragments also undergo collisional evolution, causing large particles to be disrupted and transformed into swarms of smaller fragments. While the orbital dynamics is deterministic, collisions are modeled as a stochastic process. Our bodies are assumed to thermally radiate in space as blackbodies. For the size of particles assumed in this work, the equilibrium temperature closely follows $\propto 1/\sqrt{r}$ (with the heliocentric distance defined as r).

Our model also allows us to simulate how the particle population would appear in observations of a space-based infrared telescope in orbit around the Earth or the Sun. The telescope is defined by its heliocentric position and the technical parameters of its detector (e.g., the wavelength of the recorded radiation). Observations are defined by the pointing direction and viewing angle of the telescope. By scanning at different telescope orientations, we can produce global maps of the infrared flux for the entire particle population. These virtual observations are determined at different times after the parent body's breakup to characterize the changing morphology of the particle population and its transition from trail to band structure. Our method is described in greater detail in §§ 2.1–2.5.

2.1. *The Source Population of Particles*

Our simulations start with an initial population of particles produced by the disruption of the parent object. We characterize this population using a size distribution, with $N(>D)$ the number of particles larger than diameter D. In practice, we use a power law distribution $N(>D) = N_0 D^{-\gamma}$ with a single exponent γ in the range $D_1 \leq D \leq D_2$, where D_1 and D_2 are the diameters of the minimum and maximum size particles in the model distribution, respectively.

The lower size cutoff is set to $D_1 = 25$ μm for two reasons. First, this size prevents the number of particles in the population from growing unmanageable. Second, this value corresponds to typical observations in mid-infrared band near 25 μm where particles with $D_1 \gtrsim 25$ μm have large emissivity. Note, however, that particles down to $D_1 \sim 5$–10 μm can also contribute to the mid-infrared flux because of their initially large cross section (if $\gamma > 2$). We thus studied how the trail dispersal timescale depends on D_1 by performing numerical tests with $D_1 = 10$ μm and by using analytic arguments. We find that the trail dispersal timescale reduces by a factor of few for smaller values of D_1 (see § 3.1.3). On the other hand, because of the efficient depletion of small particles by radiation forces we find that D_1 has only a small effect on the evolution of observed infrared structures at later stages, especially during the formation of dust bands.

The upper cutoff value D_2 was set as a function of the age of the disruption event (t_{age}); specifically, we set D_2 so that the particles with $D \geq D_2$ do not disrupt in t_{age}. Note also that $D \geq D_2$ have a small cross section for $\gamma > 2$ and they are unlikely to significantly contribute to the fragment swarm's mid-infrared flux. Using the particle disruption model of Grün et al. (1985) and t_{age} of ∼500 kyr, we obtain $D_2 \sim 2$ cm. The value of the power-law exponent γ is unknown a priori because laboratory shot experiments into cm size targets show a wide range of outcomes depending on factors such as projectile size, impact velocity, target strength, and impact angle (e.g., Holsapple et al. 2002). For lack of a better choice, we nominally used $\gamma = 2.5$, a value commonly seen in collisionally evolved systems (e.g., Dohnanyi 1969; O'Brien & Greenberg 2003). To be cautious, however, we also ran simulations with $\gamma = 2$ and noticed no substantial difference in the results; analysis of different, especially steeper, γ values is computationally prohibitive with our possibilities at this moment and should be checked in further work.

The number of particles released at the source must be larger than $\sim(D_2/D_1)^\gamma$ in order to guarantee that at least one particle in the population is $\sim D_2$ in diameter. Using our values of D_1, D_2, and $\gamma \sim 2.5$, each of our simulations used about 10^7 source particles. During the simulation, we followed the detailed orbital and collisional evolution of every particle, regardless of whether it was an original source particle or a fragment produced by the collisional cascade (see § 2.3). Such an approach is computer time expensive and, with the current technology, it allows only a limited number of tests to probe parameter dependence of the results.

To keep things simple, we assumed that all particles were initially ejected with zero initial velocity with respect to the disrupted parent body. We justify this assumption using the rationale of Sykes & Greenberg (1986), who found that the effect of the initial velocity field on dust band formation may be negligible when compared to radiation pressure-induced dispersion. Recall that the ejection velocities for most bodies escaping an asteroid disruption event are generally comparable to the escape velocity of the parent object; this means the breakup of a $D < 10$–20 km body should have ejected most of its ejecta at speeds of at most a few tens of m s^{-1} (see Nesvorný et al. 2006b; Nesvorný & Vokrouhlický 2006). We accounted for changes in osculating orbital elements due to effects of radiation pressure (e.g., Dermott et al. 2001). These changes are a by-product of energy and angular momentum conservation, where the gravitational force of the Sun, which is felt by each particle, is effectively weakened by the outward radiation pressure.

2.2. Orbital Propagation

2.2.1. Planetary Perturbations

Because our dynamical code has to track the evolution of hundreds of millions of particles within a single simulation, we cannot use precise numerical integration methods that require the use of an integration time step on the order of a small fraction of an orbital period. Planetary dynamists, who have long dealt with problems of this nature, have found that the principal long-term evolution of most solar system bodies can be described using a secular system of dynamical equations where all short-period frequencies are analytically eliminated. As an example, this approach was used by Laskar (1997) to numerically track the planetary orbits over Gyr timescales. In general, the advantage is using the secular equation formalism is that computation speed is $\sim 10^3$ times faster than that of the nonaveraged N-body system.

Here we adopt the same technique in order to track the orbital evolution of interplanetary dust particles (IDPs) originating in the main belt region. The simplest variant of IDP motion, derived using linearized perturbation theory (e.g., Brouwer & Clemence 1961), can readily be worked out in analytic terms assuming they have small eccentricities and inclinations. The problem, however, is that most IDPs have non-negligible values of eccentricity and inclination; this prevents the linear theory from producing accurate results. More importantly, the effects of radiation forces cause main belt IDPs to drift inward toward the Sun and cross several important secular resonances (e.g., the ν_6 and ν_{16} resonances at the inner edge of the main belt; see, e.g., Grogan et al. 2001; Dermott et al. 2001, 2002b; Kehoe et al. 2002). Linearized theory cannot reproduce the orbital evolution of IDPs close to these resonances. After experimenting with different techniques, we opted to model IDP evolution using a more elaborate variant of the secular theory. We eliminated from our equations of motion the short-period perturbations with timescales characteristic of the orbital revolution about the Sun and included fundamental

nonlinear perturbation terms (see Vokrouhlický & Farinella [1998] for a similar approach).

Although there are many possible ways to parameterize the orbit, we found it convenient to work with the following complex and nonsingular elements:

$$z = e \exp(\iota\varpi) = k + \iota h, \tag{1}$$

$$\zeta = \sin\frac{I}{2}\exp(\iota\Omega) = q + \iota p, \tag{2}$$

where $\iota = \sqrt{-1}$ (e.g., Duriez 1982; Laskar 1985) and ζ is defined with respect to the ecliptic plane. We complemented them using the value of semimajor axis a that is constant in the secular theory but changes in our model from radiation effects (§ 2.2.2). Correcting a small misprint in previous works, we obtain the averaged Lagrange equations of the following form:

$$\frac{dz}{dt} = \frac{\iota}{na^2}\left[2\eta\frac{\partial R}{\partial\bar{z}} + \frac{z}{2\eta}\left(\zeta\frac{\partial R}{\partial\zeta} + \bar{\zeta}\frac{\partial R}{\partial\bar{\zeta}}\right)\right], \tag{3}$$

$$\frac{d\zeta}{dt} = \frac{\iota}{2na^2\eta}\left[\frac{\partial R}{\partial\bar{\zeta}} - \zeta\left(z\frac{\partial R}{\partial z} - \bar{z}\frac{\partial R}{\partial\bar{z}}\right)\right], \tag{4}$$

where $\eta = (1 - z\bar{z})^{1/2}$. To include the role of radiation forces, namely that of sunlight pressure, we note that $n^2a^3 = Gm_\odot(1-\beta)$, where β is a constant that is used to characterize the effect of radiation on the body (e.g., Dermott et al. 2001). Since the variables z and ζ are noncanonical, the system of equations (3) and (4) does not have a Hamiltonian form. This inconvenience is worth the extra effort, however, because we can then use a simple form of the perturbing function R that includes planetary effects on the orbit of the particle. This form is also easily accessible in the literature. For example, up to the second order in z and ζ powers we have

$$R_{\text{lin}} = \sum Gm_j\Big[N_j\big(z\bar{z} + z_j\bar{z}_j\big) - P_j\big(z\bar{z}_j + z_j\bar{z}\big)$$
$$- 4N_j\big(\zeta\bar{\zeta} + \zeta_j\bar{\zeta}_j - \zeta\bar{\zeta}_j - \zeta_j\bar{\zeta}\big)\Big], \tag{5}$$

where m_j is the mass of jth planet and the functions

$$N_j = \frac{1}{8a_j'}\alpha_j b_{3/2}^{(1)}(\alpha_j), \tag{6}$$

$$P_j = \frac{1}{8a_j'}\alpha_j b_{3/2}^{(2)}(\alpha_j) \tag{7}$$

are expressed in terms of Laplace's coefficients $b_s^{(j)}$ with $a_j' = \max(a, a_j)$ and $\alpha_j = \min(a, a_j)/\max(a, a_j)$ (a_j is the semimajor axis of the jth planet orbit). The dependence of nonsingular elements (z_j, ζ_j), corresponding to the jth planet, can be represented by a finite Fourier series with frequencies and amplitudes derived by numerically integrating the orbits of the planets. For this work, we numerically integrated all planets for 6.6 Myr and analyzed the series of (z_j, ζ_j) using the Fourier-transform-based method of Šidlichovský & Nesvorný (1997). The upper frequency cutoff was chosen to be $300''$ yr^{-1}, such that the terms corresponding to the great inequality (i.e., induced by the nearby 5/2 mean motion resonance between Jupiter and Saturn) were not included. Compared to the main secular terms, their effect on nonsingular elements of Jupiter and Saturn is small and can be neglected for our purposes. We represent (z_j, ζ_j) of each planet by the 25 principal spectral lines whose frequencies, amplitudes, and phases are very similar to those given in Laskar (1988).

The actual perturbing function R included in our analysis goes beyond the linear approximation (eq. [5]) by assuming

$$R = R_{\text{lin}} + R_{\text{nonlin}}, \qquad (8)$$

where the nonlinear secular component R_{nonlin} includes the fourth-order terms in $(z, \zeta; z_j, \zeta_j)$ (and their complex conjugates). We took these terms from Brouwer & Clemence (1961, chapter 15). Higher order Laplace coefficients and their derivatives needed for R_{nonlin} evaluation were obtained by recurrence relations starting from

$$b_{1/2}^{(0)}(\alpha) = \frac{4}{\pi} K(\alpha), \qquad (9)$$

$$b_{1/2}^{(1)}(\alpha) = \frac{4}{\pi} \frac{K(\alpha) - E(\alpha)}{\alpha}. \qquad (10)$$

Here E and K are complete elliptic integrals of the first and second kinds.

The secular theory described here cannot be used when the orbits of IDPs and massive perturber (planet) cross each other because this causes the perturbing function R to diverge. In a Laplace-type description of R, this occurs at specific zones of semimajor axis a/a_j and eccentricity e space described by Sundman's criterion (e.g., Ferraz-Mello 1994). While the particles in our simulations are started in the main belt away from the planets, radiative forces (see § 2.2.2) cause them to migrate toward the Sun, which eventually places them on crossing orbits with the terrestrial planets. Fortunately, we do not have to account for orbit crossing with massive terrestrial planets such as Earth and Venus because the scanning regime of space-based infrared observations (§ 2.5) typically does not look inside Earth's orbit. We always terminate IDP evolution in our code when $a < 1.2$ AU (or when time exceeds t_{age}) because (1) the existing space-based infrared telescopes like *IRAS* and *Spitzer* are equipped with detectors less sensitive to the emission wavelengths of IDPs with high temperatures, and (2) IDPs are likely to have dispersed orbits inside Earth's orbit. This still leaves us with the problem that most IDPs cross the orbit of Mars at $a_j \sim 1.52$ AU. Fortunately, the mass of Mars is relatively small (its Hill's radius is only ~ 0.007 AU) and the majority of drifting IDPs are only marginally affected by its gravity. To confirm this point we tracked the evolution of particles over Mars' orbit with direct *N*-body codes (e.g., Nesvorný et al. 2006c). As an example, starting from location of the Datura cluster (§ 3.1) we found a satisfactory agreement between numerically propagated orbits and results of our secular theory for particles smaller than ~ 100 μm. More slowly drifting particles, larger than this threshold, showed some differences in orbital evolution, but we believe that those do not compromise our conclusions (a sample of integrated orbits might be found in the Online material available through our Web page[2]). Therefore, we exclude direct perturbations from Mars in the simulations presented in this work.

We also stress that our current model does not include effects of the mean motion resonances with Jupiter. These were found to be important for migrating particles from the outer parts of the main asteroid belt (e.g., Kehoe et al. 2002). We note, however, that while these resonances can modify the eccentricity vector z, they only have very limited influence on the inclination vector ζ, which controls the initial trail dispersion. Therefore, the Jovian resonances have only a small effect in our application. Their evolution from trails to bands might be affected by this fact, but we reserve this topic for future work. Similarly, our method

does not currently allow us to include the effects of the exterior mean motion resonances with the Earth. While being thus unable to reproduce fine structures such as the resonant ring exterior to the Earth (e.g., Dermott et al. 1994, 2001), this omission does not corrupt our estimates of dust trail dispersal timescale.

2.2.2. *Poynting-Robertson Drag*

To adequately describe secular dynamics of small IDPs we need to account for the effects of nongravitational perturbations, including (1) direct radiation pressure, which slightly modifies the effective solar gravity; and (2) P-R drag. For the latter we use the orbit-averaged formulation of Wyatt & Whipple (1950), which yields

$$\frac{da}{dt} = -\frac{C}{a} \frac{5 - 3\eta^2}{\eta^3}, \qquad (11)$$

$$\frac{dz}{dt} = -\frac{5}{2} \frac{C}{a^2 \eta} z, \qquad (12)$$

where $C = 3L_\odot / (8\pi \rho D c^2)$. Here, $L_\odot$ is total solar luminosity, ρ bulk density of the particle, D its diameter, and c is the velocity of light. We used $\rho = 2.5$ g cm^{-3} in our calculations. We also increased C by 30% to account for the drag produced on IDPs by their interaction with solar wind particles.

Equations (3), (4), (11), and (12) were integrated using a simple Runge-Kutta (midstep) second-order method with a fixed time step $dt = 200$ yr. We have compared the results of several test integrations with those produced by numerical integration using an *N*-body code. While the secular theory is unable to reproduce the occasional capture of some IDPs in exterior mean motion resonances with Earth and the other terrestrial planets, it does do a good job in describing the underlying secular evolution. In particular, the perturbing effects of the ν_6 and ν_{16} secular resonances are nicely reproduced for fast-drifting particles (with diameters $D \leq 500$ μm). The comparison become worse for sources with large value of inclination and/or eccentricity (such as the Emilkowalski family; § 3.4), but it is still acceptable for our purposes. Results of our test runs for single particles can be found in the online material (see footnote 2).

2.3. *The Collisional Evolution Model*

On their way toward the inner solar system, some IDPs can be collisionally disrupted. This produces swarms of smaller fragments that continue migrating inward at a faster rate. We track this evolution using a statistical collision code that was originally formulated by Vokrouhlický & Farinella (2000) and later used by Nesvorný et al. (2006c) and Farley et al. (2006).

In the code, we assume that IDPs initially released from asteroid disruption events in the main belt are only a small fraction of the total IDP population in the main belt and as such is suitable for studying the breakup of the small parent body asteroids considered here. As a result, the collisional lifetime $\tau_{\text{coll}}(D, r)$ for a particle with size D and heliocentric distance r is given by a steady state model (e.g., Grün et al. 1985). In particular, we use the Grün et al. "interplanetary" dust disruption model for $\tau_{\text{coll}}(D, r)$ that has been developed based on constraints provided by Earth-bound and interplanetary satellite measurements. The most distinctive feature of $\tau_{\text{coll}}(D, r)$ is the functional minimum at $D \sim 2$ mm where $\tau_{\text{coll}} \sim 50$ kyr at $r \sim 2.5$ AU. IDPs with smaller or larger sizes than this D have longer τ_{coll}. The short τ_{coll} value for $D \sim 2$ mm corresponds to the relative overabundance of ~ 100 μm particles found to have produced microcraters in lunar samples (Grün et al. 1985)
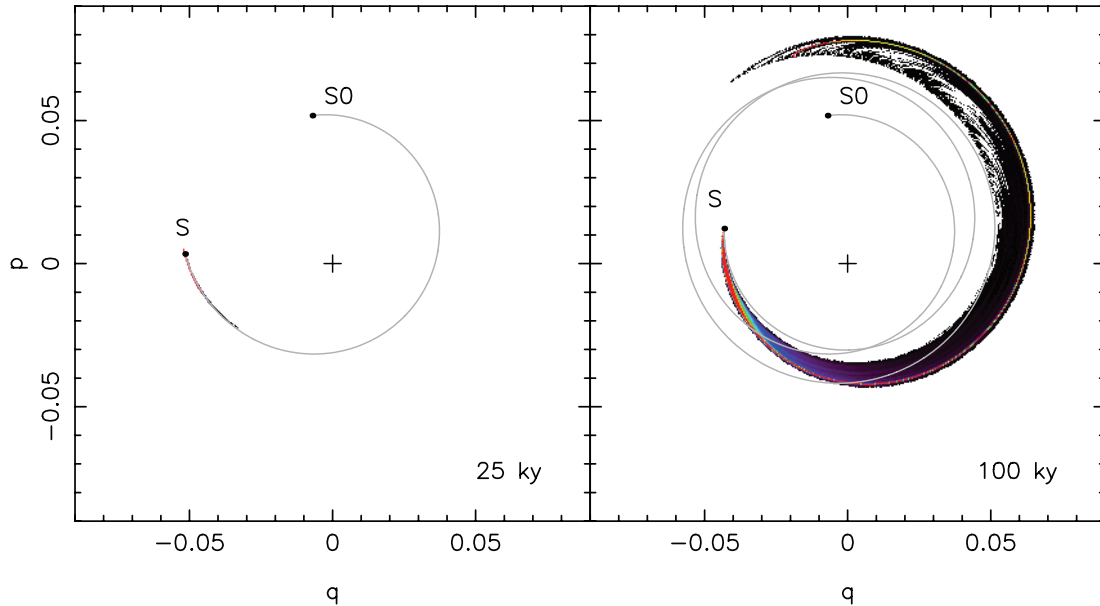
---

[2] See http://sirrah.troja.mff.cuni.cz/~davok.

FIG. 1.—Distribution of nonsingular inclination complex vector values $\zeta = q + \imath p = \sin(I/2) \exp(\imath \Omega)$ for particles released from the source event of the Datura cluster. *Left*: 25 kyr after the initial breakup. *Right*: 100 kyr after the initial breakup. We weight each particle contribution in each cell of the (q, p) plane by its cross section and sum up over the population of particles residing in the cell. White regions have no particles. Black to brighter colors (up to red) indicate values of ζ where the highest cross section of the population is located. S0 and S indicate positions of the source at time $t = 0$ and the epoch of the frame. The light gray line shows the evolution of the source in the (q, p) plane.

as well as impacts on the *Long-Duration Exposure Facility* (*LDEF*) in Earth orbit (Love & Brownlee 1993) and other spacecraft (Divine 1993). We note that for moderately large breakups up to a Karin scale, the effect of mutual collisions between the source particles is diminished by small relative encounter velocities and our approach is still applicable.

The orbits of the IDPs are dynamically propagated according to the formalism described in § 2.2. At each time step we test for collisional breakup events among individual IDPs by comparing dt/τ_{coll} to a random number ξ: if $\xi < dt/\tau_{\mathrm{coll}}$ the particle is disrupted and replaced with a swarm of fragments (the time step dt is chosen such that $dt/\tau_{\mathrm{coll}} < 0.01$ for any particle in the population). This fragment population is assumed to have a size frequency distribution extending from the largest fragment, having mass equal to half of the parent IDP, down to D_1, the smallest body of interest in our code, and is characterized by a single power-law function with cumulative index $\gamma_f = 2$. The value of γ_f follows from the conservation of mass (e.g., Greenberg & Nolan 1989). The number of IDPs processed by the code in a single simulation is roughly an order of magnitude larger than the number of original population particles (typically $\sim 10^8$ IDPs).

Note that our choice of $f = 1/2$ for the mass ratio between the largest fragment and the parent body is but one possible outcome for catastrophic disruption events. Data from the asteroid families and laboratory experiments, however, show that f may span a range of values roughly between 0.1 and 0.5. Adopting a single-slope power-law distribution, we would then have $\gamma_f = 3/(1 + f)$ with a maximum value of three for $f \rightarrow 0$. We believe that none of our results would be fundamentally changed if γ_f varied in individual breakups between 2 and 3. Such generalizations are, however, beyond the scope of the current paper.

2.4. Thermal Radiation of the Particles

While in space, IDPs are assumed to rotate rapidly enough that their radiation can be approximated by that of an isothermal sphere of size D and emissivity $\epsilon(\lambda, D)$ (λ is wavelength). As a result, the infrared flux density F (per wavelength interval $d\lambda$) at distance d from the particle is given by

$$F(\lambda) = \epsilon(\lambda, D) B(\lambda, T) \left(\frac{D}{d}\right)^2, \quad (13)$$

where $B(\lambda, T)$ is the Planck function. Particle temperature T is determined from the balance of the absorbed and reradiated energies in optical and thermal wavelengths:

$$(1 - A)\frac{S_0}{r^2} = 4 \int_{\lambda} d\lambda \, \epsilon(\lambda, D) B(\lambda, T). \quad (14)$$

Here, $S_0 \simeq 1367$ W m^{-2} is the solar constant, A is the particle albedo in the optical wavelength band (~ 0.1), and r is the heliocentric distance in AU (the factor 4 in front of integral on the right-hand side appears because the IDP absorbs light within its cross section but radiates energy over its entire surface).

Given the IDPs material parameters, we could compute emissivity ϵ using Mie theory. Within the context of this paper, however, we assume that the IDPs are large enough to act as blackbody emitters: $\epsilon \simeq 1$ in the wavelength range of interest. This means that equation (14) yields $T \simeq 280/\sqrt{r}$ K. This expression can be used in equation (13) to estimate the IDP's infrared flux density.

2.5. Synthetic Observation Model

The orbital and collisional models described above provide information about IDP orbits (a, z, ζ) at any given moment of time. However, they do not tell us the precise location of each IDP in its orbit. This means we cannot model the earliest phase of trail evolution where a concentrated IDP cluster starts extending along the orbit. Given the IDP ejection speeds of $\sim$m s^{-1} to tens of m s^{-1}, this dispersal process takes $\sim 10^3$ yr. As a result, the
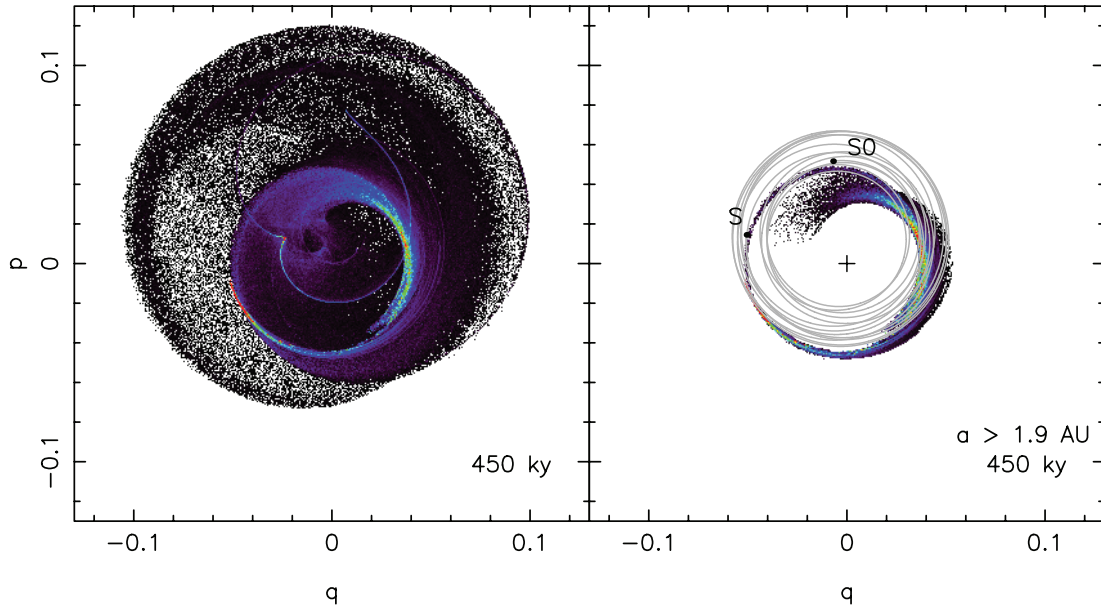
Fig. 2.— Same as in Fig. 1 but for a dust population 450 kyr after the breakup of the Datura parent body. The left panel shows all particles, while the right panel shows only those residing above the ν_{16} secular resonance (semimajor axes $a > 1.9$ AU). The light gray line shows the evolution of the source orbit in the ζ-plane between 0 and 450 kyr. The slight shift of the center of the ζ-cycles from the origin is due to the fact that the ecliptic is inclined with respect to the invariable plane of the solar system.

resolution of the secular theory results cannot be better than this timescale and we can use $\sim(200-500)$ yr as a typical time step of propagation of our model.

When an IDP's $e > 0$, the distribution of particles is highest near apocenter. The probability distribution function $\Pi(v)$ of finding particles at different values of true anomaly v is given by

$$\Pi(v) = \frac{\eta^3}{2\pi} \frac{1}{(1 + e \cos v)^2}, \qquad (15)$$

where $\eta = (1 - e^2)^{1/2}$ as before and $\Pi(v)\,dv$ is the probability that a given IDP resides between true anomaly values v and $v + dv$. Using this distribution, our synthetic space-based infrared telescope collects, at any given time, radiation from IDPs unevenly distributed along elliptic orbits. This approach is more precise than the one used in previous synthetic observation models (e.g., Nesvorný et al. 2006c) where the source particles were spread into three-dimensional annuli by randomizing their pericenter and nodal longitudes. Our new model allows us to follow the increasing dispersion of Ω and ϖ, which is important for the dust trail-to-band transition.

We decided to keep the definition of the telescope/detector as simple as possible for our simulations. It is characterized by (1) heliocentric position, (2) pointing direction, (3) field of view, and (4) sensitivity in a single wavelength (25 μm in our case). The recorded flux $F_{\rm obs}$ is then

$$F_{\rm obs} = \sum_{\rm cross} F(\lambda)\Pi(v), \qquad (16)$$

where the index "cross" under the summation symbol denotes those orbits that cross the field of view, and $F(\lambda)$ and $\Pi(v)$ are from equations (13) and (15). In practice we chose a field of view of the telescope (typically $0.5° \times 0.5°$ in the simulations below) and determine which orbits intersect it. We then compute, for the particle in the center of the field of view, its distance from the Sun

and the telescope and determine its true anomaly v. These parameters are used to calculate F and Π that contribute to the flux in equation (16). By cumulating the flux over all available orbits at the specified epoch we compute $F_{\rm obs}$. We note that the resulting flux scales with the number of particles released from the source and thus has only relative meaning unless the source population can be absolutely calibrated.

Our code could apply many different observational schedules to our synthetic telescope. We opt for the all-sky scanning at a constant 90° leading solar elongation during a 1 yr cycle. This scheme is similar to those used for trailing/leading *IRAS* observations. Our results are always referenced to the ecliptic plane and
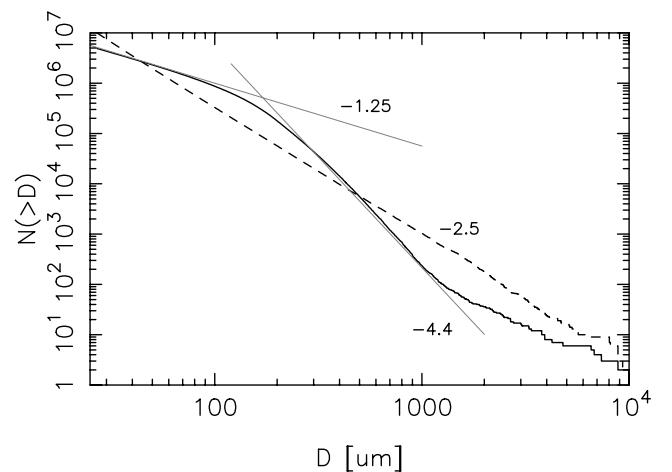

Fig. 3.— Cumulative size frequency distribution $N(>D)$ of particle diameters D (in microns) in the initial population (*dashed line*) and in the evolved population 450 kyr after the Datura parent body disrupted (*solid line*). In our simulation, the former is a power law of the form $N(>D) = N_0 D^{-\gamma}$ with $\gamma = 2.5$ (§ 2.1), while the latter is characterized by a broken power law with $\gamma \sim 1.25$ for $D \leq 100$ μm and $\gamma \sim 4.4$ for $200 \leq D \leq 1000$ μm (*thin lines*). At the largest sizes, the size distribution grows shallow because these particles only infrequently disrupt.
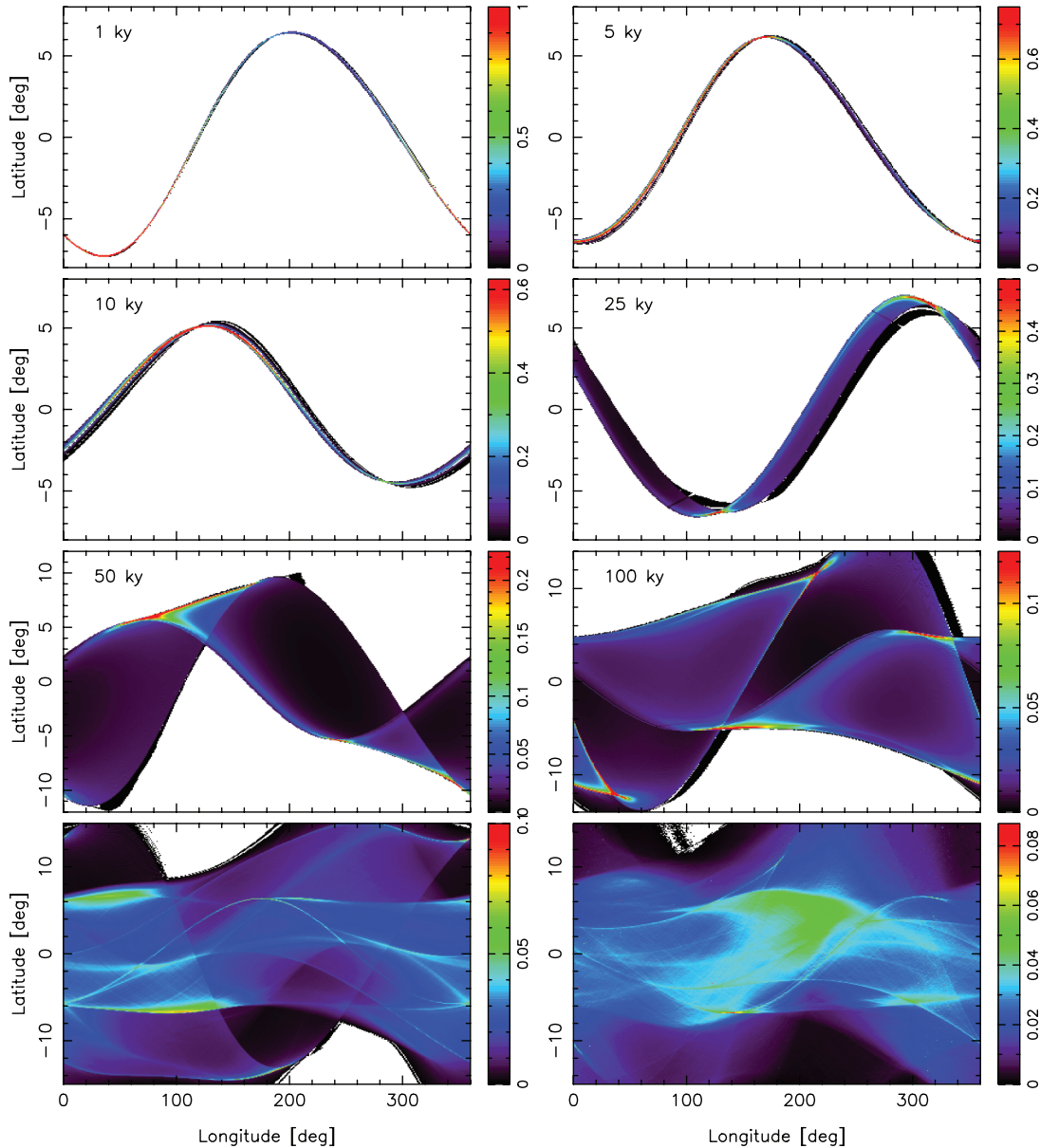
Fig. 4.—The 25 μm infrared flux from dust released by the Datura family-forming event. Simulated observations made (*from top left to bottom right*) at epochs 1, 5, 10, 25, 50, 100, 250, and 450 kyr after the parent body breakup. We assume an all-sky scanning schedule at constant 90° solar elongation; the abscissa is the ecliptic longitude and the ordinate is the ecliptic latitude of the telescope's pointing direction. The figures are a composite of 360 longitude pixels and 301 latitude pixels. The last frame, 450 kyr, corresponds to the expected infrared flux distribution of Datura dust at the present epoch (Nesvorný et al. 2006b). The color bars on the right indicate the infrared flux in arbitrary units that are the same for all frames. The color coding uses a 256 unit palette with a maximum that corresponds to the maximum flux in each frame. Note that peak flux is reduced by about an order of magnitude between the first and final frames and that the latitude range increases for later epochs as the particle population contributing to the signal disperses by interaction with the ν_{16} secular resonance.

may be directly compared with, for instance, the scans performed by the *IRAS* telescope (e.g., Sykes 1988, 1990; Nesvorný et al. 2006c).

3. RESULTS

We applied the model described above to understand how a dust trail, formed immediately after the disruption of an asteroid in the main belt, would evolve into a pair of dust bands, produced when the nodal and pericenter longitudes of the IDPs in the trail become randomized. We assumed that the source events of dust particles were the previously identified asteroid disruptions that had happened in the very recent past (see § 1). We also tested how the trail-to-band transition is affected by different heliocentric distances and inclinations of sources.

For our sources of dust, we selected the following recent breakup events in the main belt: (1) the Datura cluster, with an age of 450 ± 50 kyr (Nesvorný et al. 2006b); (2) the Emilkowalski cluster, with an age of 220 ± 30 kyr (Nesvorný & Vokrouhlický 2006); and (3) the 1992 YC2 cluster, whose age was estimated to be between 100 and 250 kyr (Nesvorný & Vokrouhlický 2006). No structures in the interplanetary dust complex have yet been associated with these potential sources. We also investigated dust evolution from the Karin cluster, whose age is 5.75 ± 0.05 Myr (e.g., Nesvorný et al. 2002; Nesvorný & Bottke 2004). Disruption of the Karin parent body is the source of a pair of β-bands found in *IRAS* data (e.g., Nesvorný et al. 2003, 2006c). These bands are one of the most distinct features in the interplanetary dust emission (e.g., Low et al. 1984; Dermott et al. 1984).
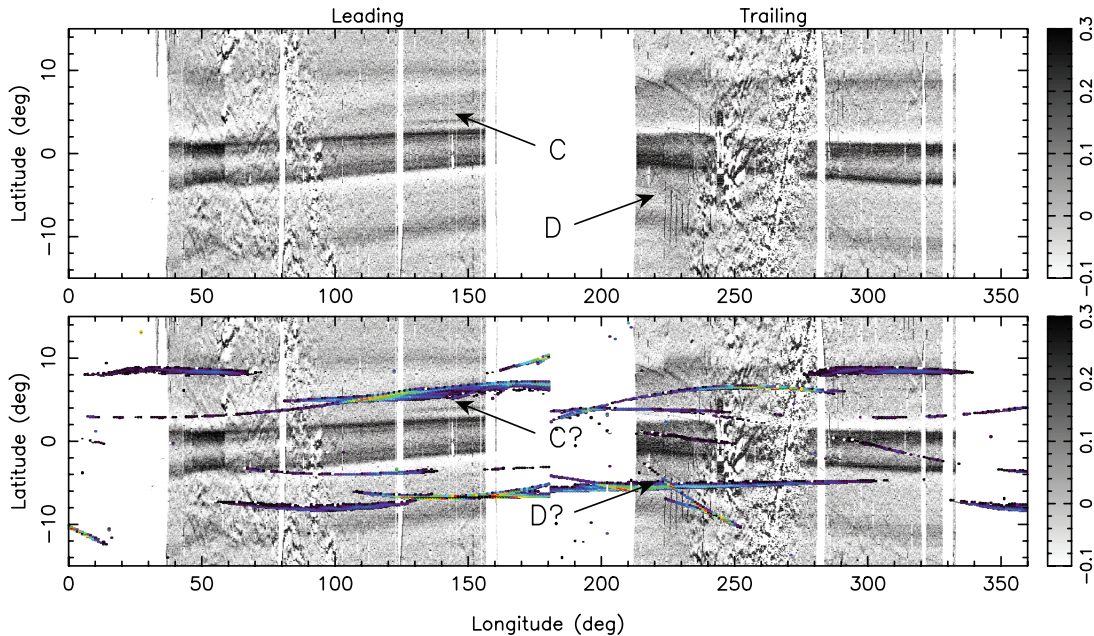
Fig. 5.— *Top and the background gray-scale map in the bottom*: All-sky map constructed from *IRAS* 25 μm observations during cycle 3 of the spacecraft's operation. Longitudes, at abscissa, smaller than 180° were observed in the leading direction, while longitudes larger than 180° were observed in the trailing direction with respect to the spacecraft heliocentric motion. The low-frequency latitude component in the data were removed by a quasi-Fourier filter with lower and upper frequency stop bands corresponding to 4° and 0.1° (e.g., Reach et al. 1997; Nesvorný et al. 2006c). This allows local features such as dust trails and bands to appear more clearly. The orphan trails C and D, discovered by Sykes (1988), are the faint structures denoted by arrows: (1) C trail extends 100°–160° longitude and 4°–7° latitude, (2) D trail extends 215°–235° longitude and −3.5° to −5.5° latitude. *Bottom, overlaid color map*: Synthetic signal of the Datura-cluster-formation dust at time 450 kyr (Fig. 4, *bottom right*) processed by the same filtering as the *IRAS* data. Solar elongation values for different latitude scans were chosen as in the *IRAS* data and they vary about 90° by approximately ±10°. The strongest emission feature in our synthetic signal roughly coincides with location of the C and D trails; the identification with the observed broader C trail is more solid than with the observed narrower and less clear D trail.

3.1. Trail/Band from the Datura Breakup Event

3.1.1. Inclination-node Dynamics of Datura IDPs

As a preamble to our analysis of infrared flux structures produced by the Datura breakup, we first examined the most relevant orbital information of the dust particles, namely the $\zeta = q + \imath p$ variable from equation (2) (recall a dust trail retains its integrity as long as IDPs have clustered values of node longitudes, while a pair of dust bands forms when node longitudes randomize in the 0°–360° interval). Figures 1 and 2 show the distribution of ζ values for the dust population released from (1270) Datura, the largest body in the Datura family with $a = 2.23$ AU, $e = 0.21$, and $i = 6.0°$, at 25, 100, and 450 kyr after the Datura breakup event took place. Note that the orbital inclination is defined as twice the distance from the center in the ζ-plane while the longitude of the node is the polar angle measured from the q-axis.

At 25 kyr, the smallest, fast-drifting particles have not yet reached the ν_{16} secular resonance at ∼1.9 AU. These smallest particles, with $D_1 = 25$ μm, have accumulated the largest nodal difference of $\Delta\Omega \sim 40°$ with respect to the source. This is in reasonable agreement with a rough analytic estimate:

$$\Delta\Omega(t) \simeq \left(\frac{\partial s}{\partial a}\right)\int_0^t \Delta a(t')dt'$$
$$= \frac{1}{3}\left(\frac{\partial s}{\partial a}\right)a_0 t \frac{1 - (a_1(t)/a_0)}{1 + (a_1(t)/a_0)}[1 + 2(a_1(t)/a_0)], \quad (17)$$

where $\Delta a(t) = a_0 - a_1(t)$, and $a_1^2(t) \simeq a_0^2 - 4Ct$ is an approximate solution of equation (11) with $\eta = 1$, and s is the proper frequency of ζ. With $D = 25$ μm, the size of the smallest IDPs in the population, $a \sim 2.23$ AU, $(\partial s/\partial a) \sim -38''$ yr^{-1} AU^{-1} (val-

ues appropriate for Datura location) and $t = 25$ kyr equation (17) yields $\Delta\Omega \sim 43°$. The estimate (17) assumes a constant value of $(\partial s/\partial a)$ along the evolutionary path of the IDPs. This assumption does not hold near the ν_{16} secular resonance location.

At 100 kyr, the smallest IDPs reached 1.2 AU and were eliminated from our simulation. Their accumulated nodal difference with respect to the source location at $t = 100$ kyr is now much larger and reaches $\Delta\Omega \sim 310°$ (Fig. 1, *right*). Except for a small dispersion, however, inclinations with respect to the ecliptic are approximately the same for all IDPs. This is because small IDPs drift so fast in a from P-R drag that the effect of the ν_{16} resonance on their orbits is limited. From Figure 1 (*left and right*), we expect that the Datura dust at 25 kyr would produce a broad trail projected onto the sky, while at 100 kyr, the structure will be more complicated.

At 450 kyr the particle population has evolved to occupy all nodal directions (Fig. 2). This is especially true for small IDPs derived from secondary breakups of larger precursors (note that the initial population of IDPs with sizes ≤150 μm has reached $a < 1.2$ AU by this time and have been removed from the simulation). Because these large precursors drift slowly by the P-R drag, their interaction with the ν_{16} resonance is stronger and their inclinations are more dispersed (e.g., Dermott et al. 2001). This allows this population of IDPs to reach a variety of inclinations (0° to ∼12.5°). The largest particles in our code, however, still reside in the inner part of the asteroid belt, forming a stream at nodal longitudes at approximately the same inclination as the source orbit (Fig. 2, *right*).

At this point, it is also instructive to compare these evolutions with those expected from the up to now neglected effect of the initial velocity-field dispersion of the dust particles. Assuming their characteristic dispersal velocity δV, large particles would
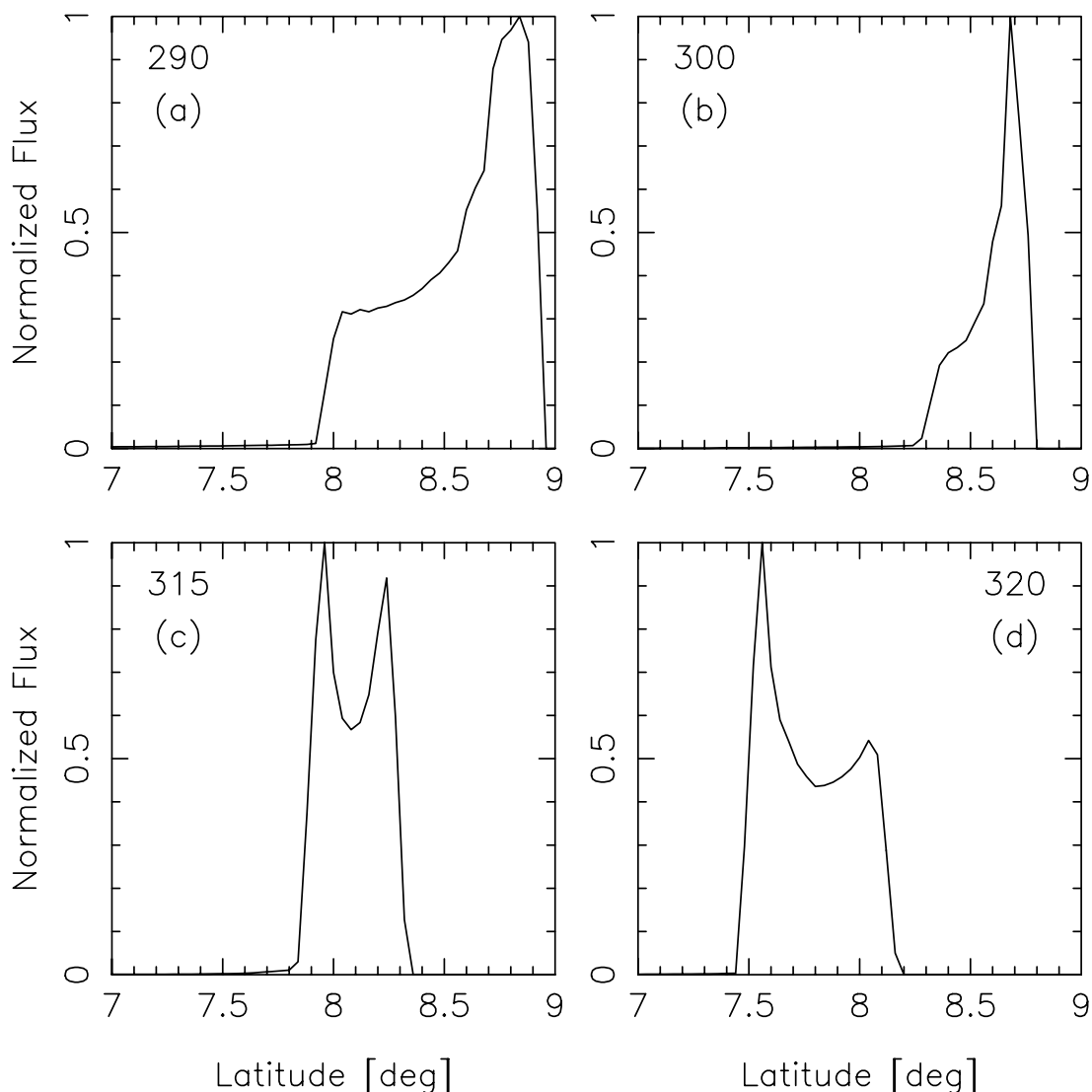
Fɪɢ. 6.—Four latitude scans of the Datura trail 25 kyr after the parent object breakup and for longitudes: (*a*) $\ell = 290°$; (*b*) $\ell = 300°$; (*c*) $\ell = 315°$; and (*d*) $\ell = 320°$. We used 115° solar elongation here. Flux is arbitrarily scaled such that the maximum is unity in each frame.

accumulate 360° nodal difference with respect to the source after time:

$$T \sim \frac{\pi}{a(\partial s/\partial a)} \frac{V}{\delta V}. \qquad (18)$$

Here V is the orbital velocity at the source at the heliocentric distance a. For the Datura cluster $\delta V \sim 2$ m s^{-1}, corresponding to the observed dispersal velocity of the largest fragments (e.g., Nesvorný et al. 2006b), and $V \sim 20$ km s^{-1} we obtain $T \sim 75$ Myr. Even with $\delta V \sim 100$ m s^{-1}, $T > t_{\rm age}$. We may thus conclude that, for small sources in the inner part of the asteroid main belt, the initial dispersal of the particle cloud produces effects on the trail evolution that are much smaller than those driven by radiation drags. We also note that $s \propto a^{5/2}$ (e.g., Fig. 1 in Vokrouhlický et al. 2006c) and thus $T \propto 1/a^3$ rapidly decreases for sources at larger heliocentric distances in the main asteroid belt. Still, the timescale T will be large relative to the dispersion timescale of Ω by P-R drag.

3.1.2. *Size-distribution Dynamics of Datura IDPs*

The evolved dust population at 450 kyr after the initial breakup has a size distribution $N(>D)$ that is very different from the

initial population (Fig. 3). In particular, it has a shallow branch at small sizes that breaks into a steeper slope between $D \sim 200$ μm and 2 mm. The shallow segment was primarily produced by small IDPs drifting toward the Sun more quickly by P-R drag than larger IDPs and thus being more readily eliminated from the population, and to a lesser extent by disruption events among the IDPs in our code produce particle swarms with $\gamma_f = 2$ (shallower than the initial population at the source). The steep part is produced by the short collisional lifetimes of $D \sim 2$ mm dust particles (Grün et al. 1985). As a consequence, the total cross section of Datura dust at 450 kyr is dominated by $\sim$(100–200) μm particles. We find it interesting how quickly the initial size distribution has been modified. The size distribution of an evolved particle population started with an initial value of $\gamma = 2$ is similar to that shown in Figure 3.

3.1.3. *All-sky Infrared Structures from Datura IDPs*

Figure 4 shows several snapshots in time of the simulated all-sky observations of dust particles released from the Datura cluster event (i.e., 1, 5, 10, 25, 50, 100, 250, and 450 kyr after the disruption). As discussed above, the initial dust trail becomes dispersed as a result of differential nodal precession of IDP orbits that reach
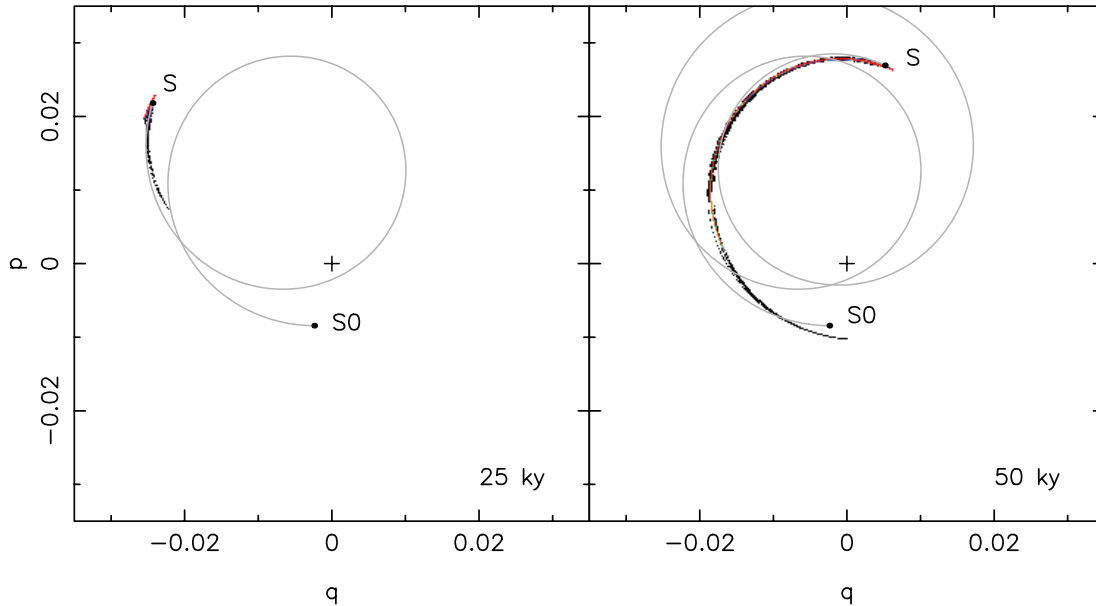
FIG. 7.—Distribution of nonsingular inclination complex vector values $\zeta = q + \imath p = \sin(I/2) \exp(\imath\Omega)$ for particles released from the Karin family breakup event at epochs 25 kyr (*left*) and 50 kyr (*right*). We multiplied the particles' number in each cell of the (q, p) plane by their cross section. No particles reside in the white regions, while black to brighter colors (up to red) show where the highest cross section of the population is located. The light gray lines show the evolution of the source (q, p). The initial and final positions of the source are denoted by S0 and S.

different heliocentric distances over time via P-R drag as a function of their size. Based on Figure 4, we find that the trail lifetime is ~25 kyr. Up to this time, large IDPs remain close to the source and exhibit the least nodal difference with respect to it (see also Fig. 1). This result could help identify the ultimate source of the unknown trail. We also note that the apocenter/pericenter flux variation is most distinctly seen at the earliest epochs, while at ≳25 kyr it disappears as the node and pericenter positions diverge. In addition, the apocenter/pericenter flux variation diminishes by systematically lower eccentricity for ≳10 kyr and orbits of particles of all sizes (see the online material available through the URL in footnote 2).

The dispersion timescale of the trail depends on the lower cutoff D_1 of IDPs contributing to the IR flux at a given wavelength. Simulations of the initial phase of dust evolution from Datura with $D_1 = 10$ μm show that the survival time of a coherent trail shrinks by a factor 2–3 compared to the one determined with $D_1 = 25$ μm (note, we analyze a direct effect of D_1 onto our results leaving apart its putative effect on self-consistent collisional evolution of the particle swarm). This is because $\Delta\Omega \propto tf(t/D_1)$ in equation (17), where f is some function (this result can be easily obtained by noting that a_1/a_0 is a function t/D_1 argument). Thus, smaller D_1 requires proportionally smaller value of t to acquire the same value of $\Delta\Omega$. The nonlinearity of the f function compensates for the extra factor t in the above equation. This means that to probe the exact dispersal time for a trail from a given source, we first need to accurately determine the composition-dependent minimum diameter D_1 of contributing particles for given wavelength and also the size distribution of the source particles. The timescale determined with $D_1 = 25$ μm, however, provides a reasonable order of magnitude estimate being moreover an upper bound of the trail dispersal timescale.

After ~25 kyr the IR flux distribution grows increasingly complicated. Planetary perturbations (1) produce variable maximum ecliptic latitudes for the trail, and (2) induce precession of the observed structures by changing the ascending nodes of the orbits. The smallest IDPs in the population accumulate a large nodal dif-

ference (Fig. 1, *right*) so that along a given latitudinal scan, radiating particles have different phases of oscillation about the ecliptic. In general, the complicated transition phase after ~50 kyr is characterized first by the development of cusps of strong infrared radiation. Their position depends on the relative geometry between the observer and the interplanetary region occupied by the radiating dust particles (see frames for 50 and 100 kyr in Fig. 4). These features later develop into incomplete arcs (the last two frames in Fig. 4) whose association with their sources is difficult to determine. Nevertheless, up to 450 kyr in this case, the structure cannot be characterized by two distinct bands of radiation. The transitory structure at $t = 450$ kyr gives rise to two partial arcs at opposite latitudes and longitudes between $150°$ and $300°$. Their relative position suggests that they may be associated with the orphan C and D trails discovered by Sykes (1988) (Fig. 5; note the C and D structures were called "trails" by Sykes [1988] but they are arcs in our terminology; see § 1 for the proper notion of trail in our view). More detailed modeling will be needed to confirm this, especially for the D trail that seems to undergo a different progression as the ecliptic longitude changes than our modeled structure does.

Figure 4 (*last panel*) shows that the dust produced in the Datura family has not formed a clearly defined band pair structure. This result can be explained using equations (17) and (18). At the current epoch, the IDPs that pick up a substantial nodal difference with respect to the source have also drifted across the ν_{16} secular resonance, which significantly dispersed their orbits, in particular value of their orbital inclination with respect to the ecliptic. For reasonable initial velocities, δV, it takes millions of years to disperse large IDPs along a circle of constant proper inclination in the ζ-plane (eq. [18]). When large particles eventually become randomized in proper nodes, and start feeding the population of smaller particles with their breakups, the strength of the source will most likely have faded to the point that they will no longer be detectable with available IR telescopes. Our tests show that disruption events cause the total cross section of the IDP population in our simulation to significantly decrease after ~200 kyr. The peak sky-plane IR luminosity decreases even
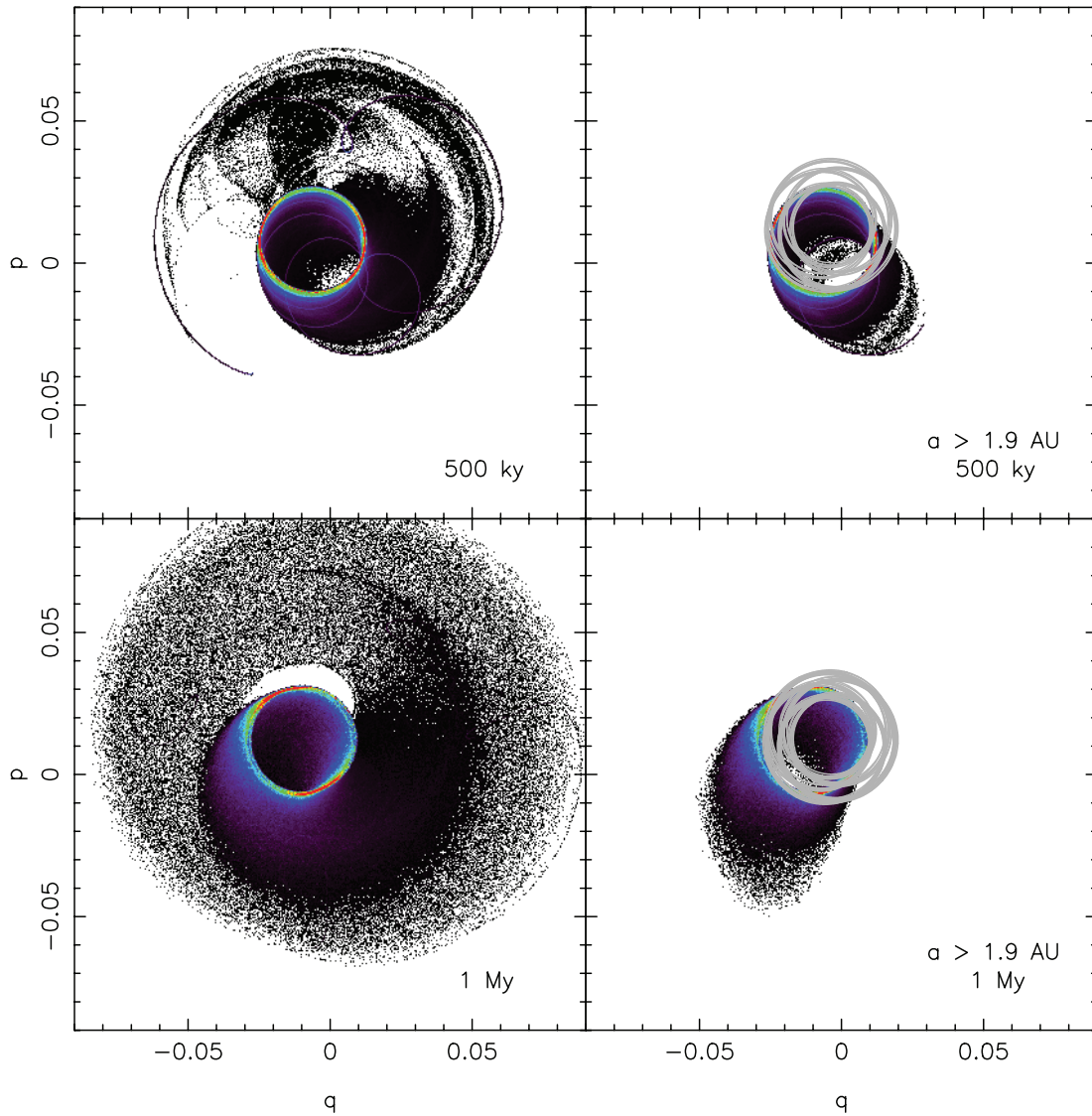
Fɪɢ. 8.— Distribution of nonsingular inclination complex vector values $\zeta = q + \imath p = \sin(I/2)\exp(\imath\Omega)$ for particles released from the Karin family breakup event at epochs 500 kyr (*top*) and 1 Myr (*bottom*). We weighted the particle population in each cell of the (q,p) plane by their cross section. No particles reside in the white regions, while black to brighter colors (up to red) indicate where the largest cross section of the population is located. *Left*: All particles. *Right*: Particles residing in the main asteroid belt with semimajor axis larger than the location of the ν_{16} secular resonance. The light gray line in the right panel shows the evolution of the source (q,p). The instantaneous circle of locations with the same proper inclination but different values of the proper longitude of node is densely populated by large particles still residing in the main belt at both epochs.

earlier ($\sim$20 kyr) as the cloud of particles becomes dispersed. As a result, Datura—and similarly small sources in the inner part of the main asteroid belt—may not create a detectable pair of dust bands in the future.

Figure 6 shows latitude scans across the Datura-formed dust trail at 25 kyr in a 30° longitude range about the brightness maximum, where we assumed 115° solar elongation. The profiles are generally double peaked with the flux ratio of the two peaks depending on the relative position of the scan to the latitude maximum of the trail emission. Two peaks in the profile are best seen at longitude $\ell = 315°$; they result from a finely tuned composition of radiation from IDPs on orbits with slightly different nodal longitudes.

Interestingly, Figure 6c is similar to the profiles reported by Nesvorný et al. (2006d) for the t1 orphan trail (see their Fig. 3, also taken at 115° solar elongation). The Datura cluster cannot be the source of that trail because of its $\sim$0.5 Myr old age, but the qualitative agreement of the profiles make us hypothesize that

the source of the t1 orphan trail (also the A trail in Sykes & Walker 1992) might be an undiscovered breakup of an main belt asteroid 10–30 kyr ago. The latitudinal smoothness of the observed t1 trail and the sharpness of our synthetic scan could be reconciled by allowing the newly released dust particles to have a small initial velocity spread.

Our results indicate that the all-sky map of the IR flux from Datura-produced dust after 450 kyr of evolution does not depend on the lower cutoff D_1. This is because the IR flux is dominated by $\sim$(100–200) μm IDPs that represent the majority of the total cross section in the population (Fig. 3). The very shallow size distribution for IDPs with $D < 100$ μm has a relatively small total cross section. Accordingly, none of our simulated flux structures depend on the exact choice of D_1 as far as $D_1 < 100$ μm.

3.2. *Trail/Band from Karin Location*

We now investigate the Karin cluster, whose larger size (parent body $D \approx 33$ km) and somewhat older age ($\sim$5.8 Myr old)
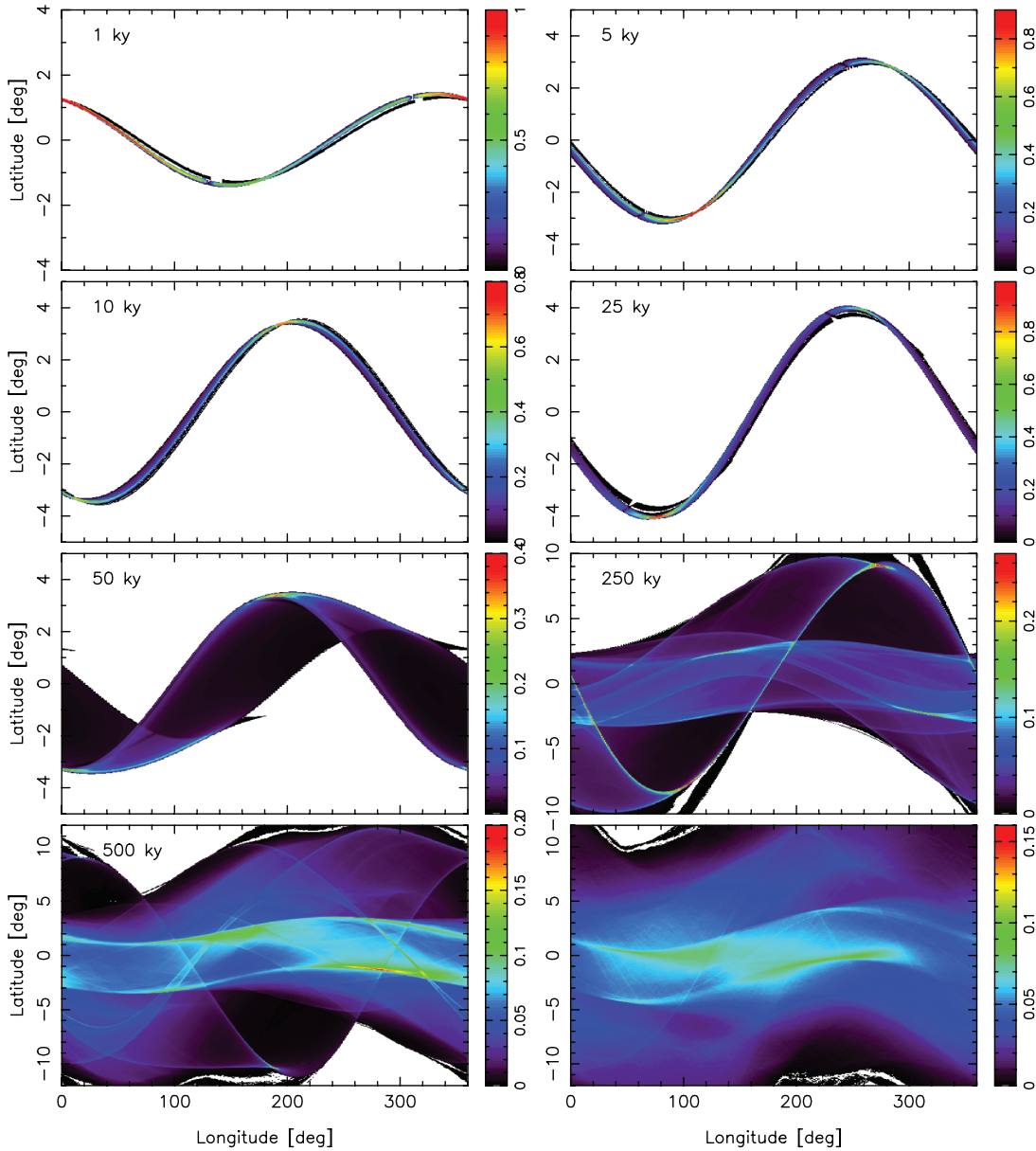
FIG. 9.—Same as in Fig. 4 but for a source provided by the breakup of the Karin parent body at 1, 5, 10, 25, 50, 250, and 500 kyr and 1 Myr (*bottom right*) after the disruption event. With estimated age of 5.75 ± 0.05 Myr (Nesvorný & Bottke 2004), the Karin family is still a factor 6 older than the epoch of the last frame. Computer limitations prevent us from extending our simulation to $t = 5.75$ Myr. A pair of dust bands nears completion at 1 Myr after the breakup. The Karin cluster is known to be a source of the prominent β-dust band (Nesvorný et al. 2003, 2006c).

allowed it to form the β-dust bands, one of the two most promi-nent band features in the interplanetary particle complex (Nesvorný et al. 2003). Nesvorný et al. (2006c) has already modeled the IDP population in these bands. Our goal here is to show how a trail produced by the Karin breakup evolved into the currently ob-served band. Computational constraints as well as the limitations of our secular theory allowed us to track the evolution of model IDPs over 1 Myr only. Longer evolution times would require us to increase the upper limit size D_2 of IDPs at the source to ~ 1 m, which in turn would increase the number of IDPs in our simula-tion to values we cannot yet handle.

3.2.1. Inclination-node Dynamics of Karin IDPs

Figure 7 shows the distribution of ζ-values for IDPs evolved from the Karin's location after 25 kyr (*left*) and 50 kyr (*right*). During this early stage of evolution, all particles in our simulation ($D \geq 25$ μm) are still located in the main asteroid belt. Longitudes

of nodes extend over $\sim 50°$ along a proper inclination circle at 25 kyr, in good agreement with equation (17) [$a \simeq 2.86$ AU and $(\partial s/\partial a) \simeq -70''$ yr^{-1} AU^{-1} for Karin]. The same compari-son at 50 kyr shows that the numerical range for the longitudes of node of the IDPs is $\sim 200°$, only slightly smaller than the $\sim 260°$ predicted from equation (17).

Figure 8 shows the distribution of ζ-values for Karin-derived IDPs after 0.5 Myr (*top*) and 1 Myr (*bottom*). There are important differences between this figure and Figure 2, where Datura IDPs were shown after 450 kyr of evolution. In all frames of Figure 8, the majority of IDPs that contribute to the total cross section of the population (100–200 μm diameters) are still in the main belt. This is because the Karin family is located at $a \approx 2.867$ AU, considerably farther out from the Sun than Datura. While in the main belt, the orbits of Karin's IDPs are less perturbed, confining their ζ-values to a circle with a radius defined by the proper incli-nation value of the source. At 0.5 Myr after the original breakup,
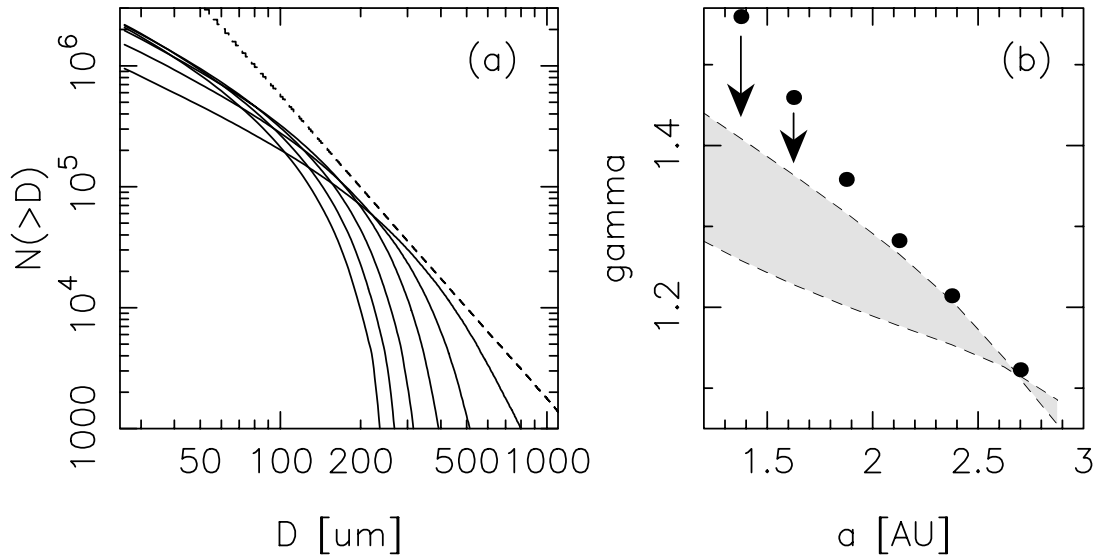
Fig. 10.—*Left*: Size frequency distribution of particles 1 Myr after the Karin parent body disruption event at different heliocentric zones with centers defined by $a_j = 1.375 + j \times 0.25$ AU ($j = 0, \ldots, 6$). Multigeneration collisional breakup events of the initial particles and removal of small particles by the P-R drag make the initial power-law initial distribution bend at $\sim(100-200)$ μm size. *Dashed line*: Assumed power-law distribution at the source. *Right*: Symbols showing power-law exponents of the particle size distribution in $D = (25-50)$ μm range in different heliocentric zones (*abscissa*) and again 1 Myr after the Karin parent body disruption event. The range of exponent values found in the model of Nesvorný et al. (2006c, their Fig. 24) is shown by the shaded area. The upper limit assumed a constant source of particles ($\tau = \infty$ in the notation of that paper), while the lower limit assumed a rapidly decaying source of particles ($\tau = 0.5$ Myr). The arrows indicate where we expect our exponents would shift if the $D = (10-50)$ μm range is used as in Nesvorný et al. (2006c). [*See the electronic edition of the Journal for a color version of this figure.*]

only the smallest particles in our simulation ($D \leq 150$ μm) could have drifted far enough to reach the location of the ν_{16} secular resonance. At 1 Myr, particles twice as large have reached the ν_{16} resonance. This means that the IDP population at smaller heliocentric distances is now more numerous and distributed in inclination and longitude of node. At the same time, fragmentation events in the main belt continue to feed the IDP population distributed along a circle of proper inclination at the source. This distribution is not uniform, partly because our simulation contains a limited number of large particles, but also because of the initial spread of submeter particles at the source (due to finite ejection velocity δV). This produces shear along a circle of proper inclination that may ultimately help create pairs of dust bands. The characteristic dispersal timescale T from equation (18) is only $\sim$2 Myr (assuming $V \simeq 17.6$ km s^{-1} and $\delta V \simeq 20$ m s^{-1}).

3.2.2. *All-sky Infrared Structures from Karin IDPs*

Figure 9 shows simulated all-sky maps of IR flux from the population of IDPs released by the Karin family forming event at times between 1 kyr and 1 Myr following the disruption. The dust trail survival timescale is once again $\sim$30 kyr. The trail width varies nonlinearly with time. For instance, the width at 25 kyr is about the same as that at 10 kyr. The reason for this may be inferred from the behavior of ζ (see Fig. 7, *left*). While the population expands in proper longitude of node (see eq. [17]) between 10 and 25 kyr, their osculating longitude of node values (i.e., the angle measured from the origin in the ζ-plane) remain confined within $\sim$50° at 25 kyr. Because the Karin family has a small inclination, such that the proper inclination is not much larger than the forced inclination, the center of the circle of constant proper inclination at the source shifts away from $(0, 0)$ in the ζ-plane (Fig. 7).

At 50 kyr the trail is already dispersed by a significant degree, and forms a structure similar to that of the Datura case. Cusps and incomplete arcs form during the transition phase $t = 50-250$ kyr. Finally, the last two frames show the completion of a pair of dust bands roughly 1 Myr after the parent body disruption.

The initial velocity dispersion of the large IDPs in the source affects the dispersion of luminosity in the bands, with larger velocities leading to more dispersed longitude values. We thus anticipate that a pair of bands comparable to those observed will fully develop between 1 and 2 Myr after the breakup of the Karin family precursor.

3.2.3. *Heliocentric Distribution of Karin IDPs at 1 Myr*

Figure 10 shows how Karin-produced IDPs are distributed at different heliocentric distances after 1 Myr. At this epoch, preceded with a phase of dynamical and collisional feeding of the inner heliocentric zones, the population of small dust particles seemed to reach equilibrium with no further evolution. The left panel shows the cumulative size frequency distribution of IDPs in several heliocentric zones (*solid lines*; the particles are grouped according to their semimajor axes values) as compared to the assumed size frequency distribution of IDPs released in the source (*dashed line*). The dashed line, which is an imposed power-law distribution with an exponent of $\gamma = 2.5$ (§ 2.1), gets modified in two ways. IDPs larger than $\sim$500 μm are short lived against collisional disruption (Grün et al. 1985) and disrupt into smaller fragments. This creates a shortage of these bodies at smaller heliocentric distances while steepening the local power-law exponent to values greater than 2.5. IDPs smaller than $\sim$100 μm have shallower size-distribution slopes than 2.5 because they readily drift inward toward the Sun. Their loss rates are high enough to overcome their replenishment via fragmentation events among larger particles.

The power-law exponents of the cumulative size frequency distribution in the 25-50 μm diameter interval after 1 Myr are shown in Figure 10b. As described above, the shallow power law index of these small IDPs is produced by two processes: (1) we assume that the cumulative size distribution of collisional fragments is a single power-law with $\gamma_f = 2$ (§ 2.3), which is shallower than the source; and (2) the effectiveness of P-R drag, which sweeps IDPs toward the Sun, is inversely proportional to the size of the particle. As a result, IDPs between 50 and 200 μm
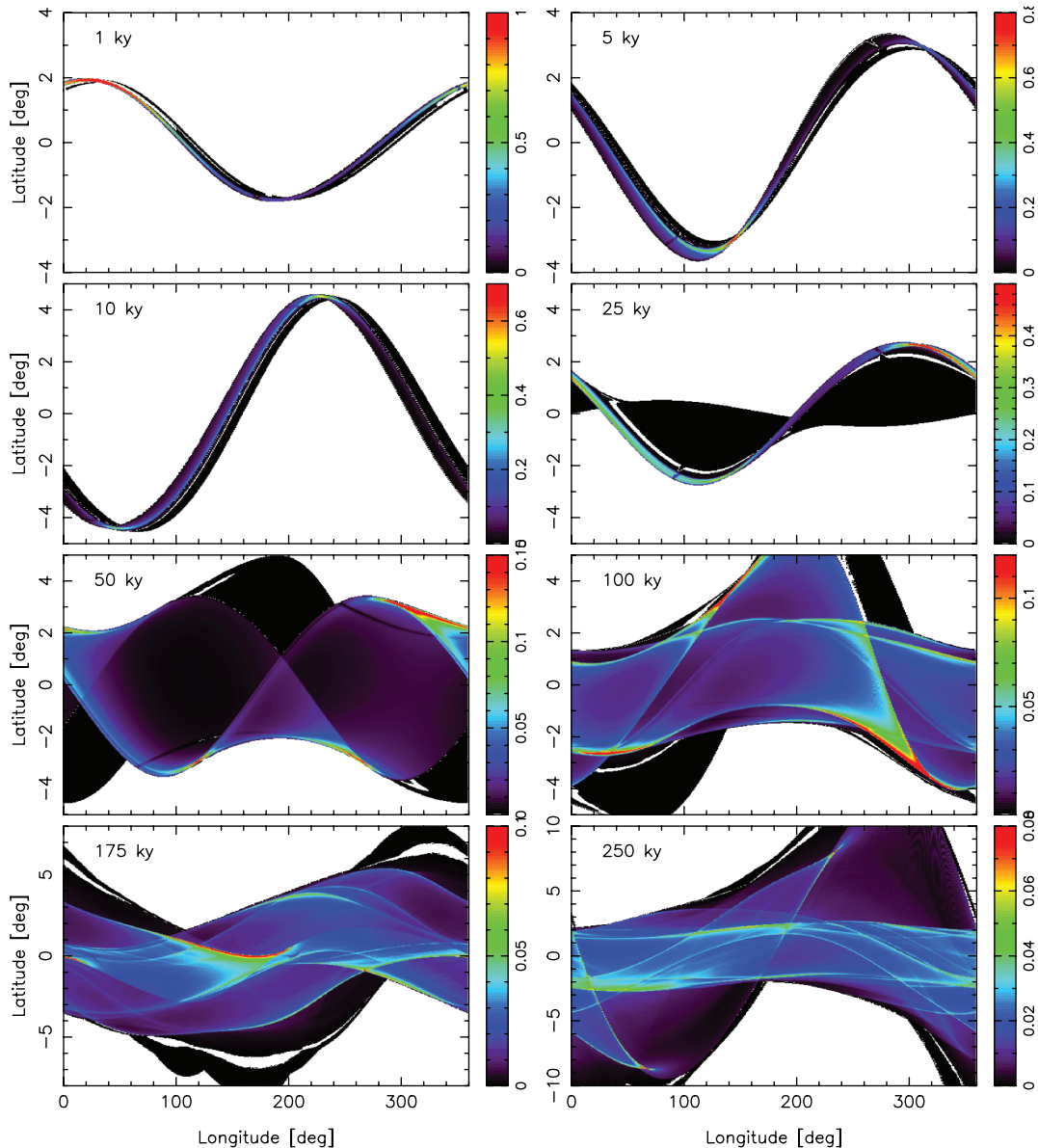
Fig. 11.—Same as in Fig. 4, but for the source given by the disruption of the parent body of the 1999 YC2 family. The sequence of epochs is: 1, 5, 10, 25, 50, 100, 175, and 250 kyr. The estimated age of this family ranges through the interval 100–250 kyr covered by the last three frames.

dominate both the total cross section and mass of the IDP populations in most of our heliocentric zones. We find also that the zone 1.75–2.25 AU contributes most to the total cross section of Karin's IDPs. This differs from theoretical predictions based on IDP evolution models that ignore collisions. These models produce a cross section that falls off linearly with heliocentric distance.

It is interesting to compare results in Figure 10 with those used by Nesvorný et al. (2006c; their Figs. 23 and 24), who used a simplified, empirical model to characterize Karin IDP populations in different heliocentric zones. Instead of releasing a large population of IDPs at the initial breakup event and tracking them to the current epoch, as we do here, they used more limited IDP populations ($D \leq 5$ mm) and assumed that the source population exponentially decayed with time by collisional grinding. Performing several simulations where their source population decayed away with different e-folding timescales, they obtained the power-law exponents located within the shaded zone of Figure 10b. In their model, the IDP populations with steep progression of power-law exponents toward small heliocentric distances occur for sources that maintain their activity nearly constant. On the other hand, the IDP populations with shallow progression of power-law exponents toward small heliocentric distances occur for fast-decaying sources (e.g., only 0.5 Myr e-folding timescale). The former case was found to provide the best fits to *IRAS*-measured profiles of the β-dust band associated with the Karin family.

Interestingly, the exponents determined in our simulations show a steep progression toward smaller heliocentric-distance zones, even slightly steeper than the steepest case in Nesvorný et al. We believe this is caused by the fact that Nesvorný et al. (2006c) used local power-law exponents of the size distribution function in the 10–50 μm diameter range, while here we use a more restricted range (25–50 μm diameters).

3.3. *Trail/Band from 1992 YC2 Location*

The 1992 YC2 family resides in the central part of the main asteroid belt ($a \simeq 2.62$ AU) and it has very low orbital inclination
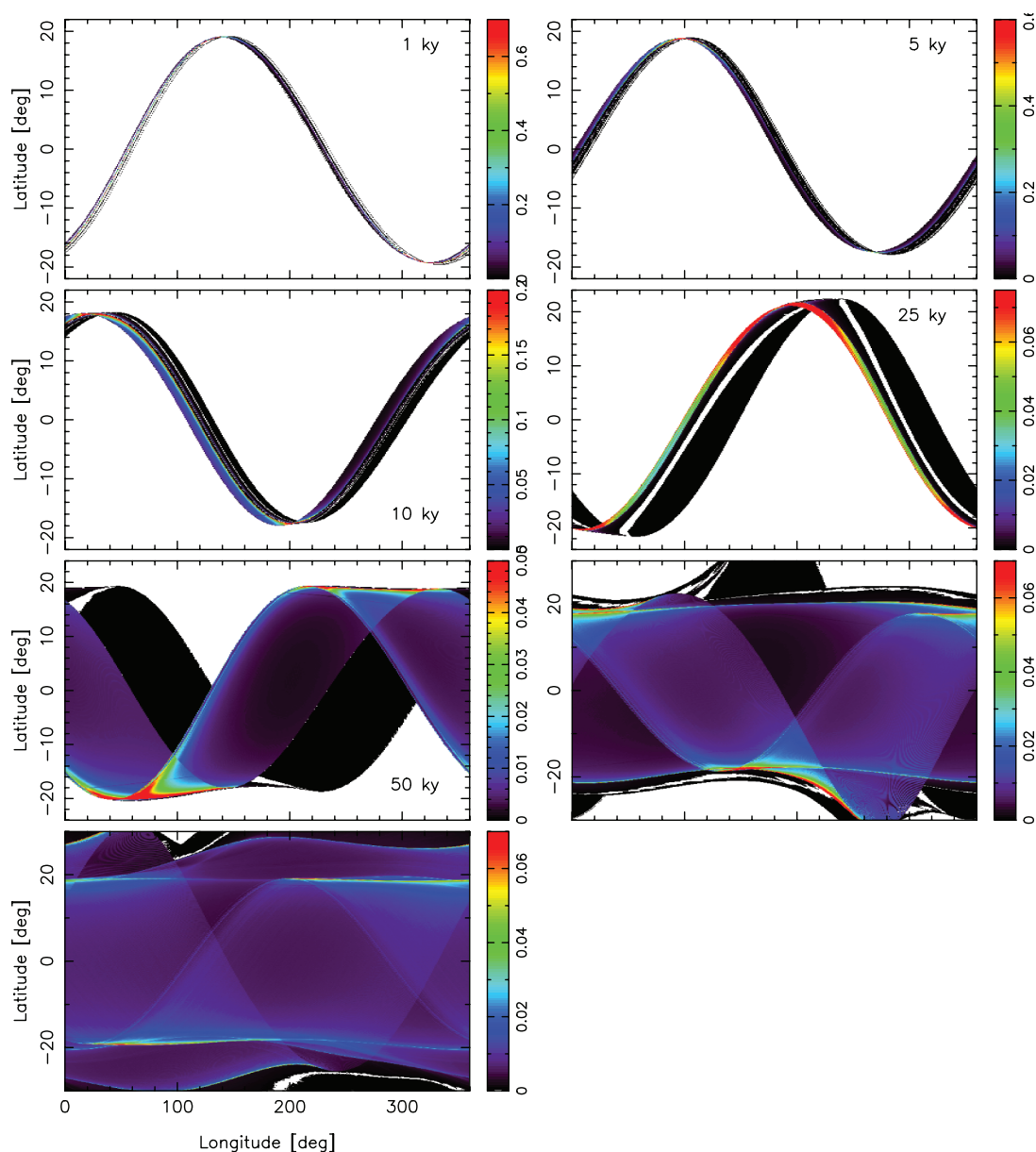
FIG. 12.— Same as in Fig. 4, but for the source given by the disruption of the parent body of the Emilkowalski family. The sequence of epochs is: 1, 5, 10, 25, 50, 100 (*third row, right*), and 220 kyr (*bottom left*). The last frame corresponds to the estimated age of this cluster (Nesvorný & Vokrouhlický 2006) and indicates two broad arcs near to their transition into bands. We note that the $\sim\pm19°$ latitude location of the arcs, instead of the $17.2°$ proper inclination of the source, is a combination of parallactic effect (telescope at 1 AU heliocentric distance) and possible inaccuracies due to limitations of our third-order secular theory for orbital propagation.

($i \sim 2.86°$ proper value). It consists of a group of three small asteroids ($D \sim 1–4$ km). The parent object likely had $D \sim 5–7$ km. The small number of known 1992 YC2 members and their inaccurate orbits made it problematic to determine the family age exactly. Nesvorný & Vokrouhlický (2006) were only able to constrain the age to a broad interval of 100–250 kyr.

Figure 11 shows snapshots of all-sky observations of IDPs evolving from the 1992 YC2–forming event between 1 and 250 kyr. Because this source is in the same heliocentric zone as Karin, and it has a similar proper inclination, the evolution shown in Figure 11 is similar to that of Figure 9.

For $t = 100–250$ kyr, the infrared flux is irregular and characterized by highly dynamic partial arc segments, not yet organized into a fully developed pair of dust bands. The similar proper inclination of the source to that of Karin means that the main IR

flux structures of the 1992 YC2 dust cloud fall to similar ecliptic latitudes as the β-dust bands (e.g., Nesvorný et al. 2003, 2006c). Since the size of the 1992 YC2 parent object was likely a factor ~5 smaller than the Karin parent body, and a factor of 20–40 smaller than Veritas, the amount of dust released in the 1992 YC2 breakup event was probably several orders of magnitude smaller than that produced by the Karin and Veritas breakups. As far as today's contribution to the interplanetary dust complex is concerned, the younger age of 1992 YC2 may partly compensate for its initially much smaller dust production. Still, we expect that the flux from IDPs released during the 1992 YC2 event is about an order of magnitude smaller than that produced by Karin IDPs. It could be interesting to analyze whether some of the major fit inconsistencies between the observed and modeled *IRAS*-scan fluxes of the β-bands could be reconciled by including 1992 YC2 as an additional source.

3.4. *Trail/Band from Emilkowalski Location*

The Emilkowalski family resides at about the same heliocentric distance as the 1992 YC2 family ($a \simeq 2.60$ AU) but its inclination is much larger ($i \sim 17.2^{\circ}$ proper value). (14627) Emilkowalski is an ~ 8.5 km diameter asteroid, while the other two members of this family have diameters of ~ 3.5 and ~ 2 km, suggesting a ~ 10 km diameter parent object. Fortunate relative geometry of their orbits allowed Nesvorný & Vokrouhlický (2006) to determine the age of this family be 220 ± 30 kyr. Figure 12 shows snapshots in time of all-sky observations of IDPs evolving from this source between 1 and 220 kyr, with the last frame corresponding to the estimated age.

Because the proper inclination of the source is significantly larger than the forced inclination produced by planetary perturbations, the later epochs are characterized by incomplete arcs at approximately the same latitude as that of the source (it is appropriate, however, to recall that our low-order secular theory of orbital propagation might not be fully adequate in this case and our results will be checked using complete numerical integrations in the future). These will eventually evolve into a pair of bands. It is not clear whether a faint pair of dust bands would be formed in the last frame (i.e., 220 kyr) if the effects of the initial velocity dispersion are included in the simulation. The ZC infrared structures at high ecliptic latitudes have yet to be studied with an instrument more sensitive than that of *IRAS* (e.g., the *Spitzer Space Telescope*). For this reason, we leave for future work a study of its specific features, but note preliminarily that weak M and/or N bands of Sykes (1988; see also Reach et al. 1997) might be good candidates for structures related to the Emilkowalski source.

4. DISCUSSION AND CONCLUSIONS

We have found that asteroid dust trails become dispersed beyond a detection threshold in $\sim(10-30)$ kyr. While this value also depends on the steepness of the initial population's size distribution function in the tens to hundreds of microns range, we find that it can be roughly obtained using equation (17). We find

that the primary effect that limits the trail's lifetime is the P-R drift of the smallest particles that contribute to that trail. This is because the timescale for small IDPs to evolve by P-R effect is shorter than both (1) the timescale to shear the IDP population via its initial velocity at the source (eq. [18]), and (2) the collisional lifetimes of particles.

The estimated trail lifetimes provide us with some interesting constraints on the parent bodies of the observed orphan trails A and B (Sykes 1988). Nesvorný et al. (2006d) interpreted them as by-products of asteroid disruption events. Bottke et al. (2005) found that a $D \sim 5-7$ km asteroid across the main belt disrupts every ~ 10 kyr. This suggests that the parent objects of dust trails A and B were produced by asteroid breakups of this size. Note that the youngest asteroid families found to date (Nesvorný et al. 2006b; Nesvorný & Vokrouhlický 2006) are still too old to produce the A and B trails. Moreover, $D \sim 1$ km breakup events that occur once per ~ 100 yr apparently do not provide enough dust to be detectable with current instruments, because *IRAS* or *Spitzer* would otherwise observe many more orphan trails.

If the parent bodies of the A and B orphan trails were produced by breakups in the $D \sim 5-7$ km range, we can use *Spitzer Space Telescope* to constrain the orbits of their source families with greater precision than was previously available. Combining this work with new all-sky asteroid surveys such as Pan-STARRS (Jedicke et al. 2007), it is our hope to find their associated asteroid families in the near future.

REFERENCES

Bottke, W. F., Durda, D. D., Nesvorný, D., Jedicke, R., Morbidelli, A., Vokrouhlický, D., & Levison, H. F. 2005, Icarus, 179, 63
Brouwer, D., & Clemence, G. M. 1961, Methods of Celestial Mechanics (New York: Academic Press)
Burns, J. A., Lamy, P. L., & Soter, S. 1979, Icarus, 40, 1
Davies, J. K., Sykes, M. V., Reach, W. T., Boulanger, F., Sibille, F., & Cesarsky, C. J. 1997, Icarus, 127, 251
Dermott, S. F., Durda, D. D., Grogan, K., & Kehoe, T. J. J. 2002a, in Proc. Asteroids III, ed. W. F. Bottke et al. (Tucson: Univ. Arizona Press), 423
Dermott, S. F., Grogan, K., Durda, D. D., Jayaraman, S., Kehoe, T. J. J., Kortenkamp, S. J., & Wyatt, M. C. 2001, in Interplanetary Dust, ed. E. Grün et al. (Berlin: Springer), 569
Dermott, S. F., Jayaraman, S., Xu, Y. L., Gustafson, B. A. S., & Liou, J. C. 1994, Nature, 369, 719
Dermott, S. F., Kehoe, T. J. J., Durda, D. D., Grogan, K., & Nesvorný D. 2002b, in Asteroids, Comets, and Meteors 2002, ed. B. Warmbein (ESA SP-500; Noordwijk: ESA), 319
Dermott, S. F., Nicholson, P. D., Burns, J. A., & Houck, J. R. 1984, Nature, 312, 505
Divine, N. 1993, J. Geophys. Res., 98, 17029
Dohnanyi, J. W. 1969, J. Geophys. Res., 74, 2531
Duriez, L. 1982, Celest. Mech., 26, 231
Farley, K. A., Vokrouhlický, D., Bottke, W. F., & Nesvorný, D. 2006, Nature, 439, 295
Ferraz-Mello, S. 1994, Celest. Mech. Dyn. Astron., 58, 37
Greenberg, R., & Nolan, M. C. 1989, in Proc. Asteroids II, ed. R. P. Binzel, T. Gehrels, & M. S. Matthews (Tucson: Univ. Arizona Press), 778
Grogan, K., Dermott, S. F., & Durda, D. D. 2001, Icarus, 152, 251
Grün, E., Zook, H. A., Fechtig, H., & Giese, R. H. 1985, Icarus, 62, 244
Hahn, J. M., Zook, H. A., Cooper, B., & Sunkara, B. 2002, Icarus, 158, 360

Holsapple, K., Giblin, I., Housen, K., Nakamura, A., & Ryan, E. 2002, in Proc. Asteroids III, ed. W. F. Bottke et al. (Tucson: Univ. Arizona Press), 443
Hsieh, H. H., & Jewitt, D. C. 2006, Science, 312, 561
Hsieh, H. H., Jewitt, D. C., & Fernández, Y. R. 2004, AJ, 127, 2997
Ishiguro, M., et al. 2002, ApJ, 572, L117
Jedicke, R., Magnier, E. A., Kaiser, N., & Chambers, K. C. 2007, in Proc. IAU Symp. 236, Near Earth Objects, Our Celestial Neighbors: Opportunity and Risk, ed. A. Milani, G. B. Valsecchi, & D. Vokrouhlický (Cambridge: Cambridge Univ. Press), 341
Kehoe, T. J. J., Dermott, S. F., & Grogan, K. 2002, Mem. Soc. Astron. Italiana, 73, 684
Kelsall, T., et al. 1998, ApJ, 508, 44
Laskar, J. 1985, A&A, 144, 133
———. 1988, A&A, 198, 341
———. 1997, A&A, 317, L75
Love, S. G., & Brownlee, D. E. 1993, Science, 262, 550
Low, F. J., et al. 1984, ApJ, 278, L19
Nakamura, A., Fujii, Y., Ishiguro, M., Morishige, K., Yokogawa, S., Jenniskens, P., & Mukai, T. 2000, ApJ, 540, 1172
Nesvorný, D., & Bottke, W. F. 2004, Icarus, 170, 324
Nesvorný, D., Bottke, W. F., Levison, H. F., & Dones, L. 2002, Nature, 417, 720
———. 2003, ApJ, 591, 486
Nesvorný, D., Enke, B. L., Bottke, W. F., Durda, D. D., Asphaug, E., & Richardson, D. C. 2006a, Icarus, 183, 296
Nesvorný, D., & Vokrouhlický, D. 2006, AJ, 132, 1950
Nesvorný, D., Vokrouhlický, D., & Bottke, W. F. 2006b, Science, 312, 1490
Nesvorný, D., Vokrouhlický, D., Bottke, W. F., & Sykes, M. V. 2006c, Icarus, 181, 107
Nesvorný, D., et al. 2006d, AJ, 132, 582
O'Brien, D. P., & Greenberg, R. 2003, Icarus, 164, 334

Reach, W. T., Franz, B. A., & Weiland, J. L. 1997, Icarus, 127, 461

Reach, W. T., Sykes, M. V., Lien, D., & Davies, J. K. 2000, Icarus, 148, 80

Šidlichovský, M., & Nesvorný, D. 1997, Celest. Mech. Dyn. Astron., 65, 137

Sykes, M. V. 1988, ApJ, 334, L55

———. 1990, Icarus, 85, 267

Sykes, M. V., & Greenberg, R. 1986, Icarus, 65, 51

Sykes, M. V., Greenberg, R., Dermott, S. F., Nicholson, P. D., Burns, J. A., & Gautier, T. N. 1989, in Proc. Asteroids II, ed. R. P. Binzel, T. Gehrels, & M. S. Matthews (Tucson: Univ. Arizona Press), 339

Sykes, M. V., Grün, E., Reach, W. T., & Jenniskens, P. 2004, in Comets II, ed. M. C. Festou, H. U. Keller, & H. A. Weaver (Tucson: Univ. Arizona Press), 677

Sykes, M. V., Lebofsky, L. A., Hunten, D. M., & Low, F 1986, Science, 232, 1115

Sykes, M. V., & Walker, R. G. 1992, Icarus, 95, 180

Telesco, C. M., et al. 2005, Nature, 433, 133

Vokrouhlický, D., Brož, M., Morbidelli, A., Bottke, W. F., & Nesvorný, D. 2006a, Icarus, 182, 118

Vokrouhlický, D., Brož, M., Morbidelli, A., Bottke, W. F., Nesvorný, D., Lazzaro, D., & Rivkin, A. S. 2006b, Icarus, 182, 92

Vokrouhlický, D., & Farinella, P. 1998, A&A, 335, 351

———. 2000, Nature, 407, 606

Vokrouhlický, D., Nesvorný, D., & Bottke, W. F. 2003, Nature, 425, 147

———. 2006c, Icarus, 184, 1

Wyatt, S. P., & Whipple, F. L. 1950, ApJ, 111, 134